



UNIVERSITAT DE  
BARCELONA

## Inversion Tectonics in the Alpine Foreland, Eastern Alps (Austria)

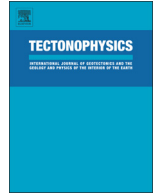
Pablo Martínez Granado



Aquesta tesi doctoral està subjecta a la llicència **Reconeixement- NoComercial – SenseObraDerivada 3.0. Espanya de Creative Commons.**

Esta tesis doctoral está sujeta a la licencia **Reconocimiento - NoComercial – SinObraDerivada 3.0. España de Creative Commons.**

This doctoral thesis is licensed under the **Creative Commons Attribution-NonCommercial-NoDerivs 3.0. Spain License.**



# Basin inversion in tectonic wedges: Insights from analogue modelling and the Alpine-Carpathian fold-and-thrust belt



P. Granado<sup>a,b,\*</sup>, O. Ferrer<sup>a,b</sup>, J.A. Muñoz<sup>a,b</sup>, W. Thöny<sup>c</sup>, P. Strauss<sup>c</sup>

<sup>a</sup> Institut de Recerca Geomodels, Universitat de Barcelona, Martí i Franquès s/n, 08028 Barcelona, Spain

<sup>b</sup> Departament de Dinàmica de la Terra i de l'Oceà, Universitat de Barcelona, Martí i Franquès s/n, 08028 Barcelona, Spain

<sup>c</sup> OMV AUSTRIA Exploration and Production GmbH, Trabrennstraße 6-8, 1020 Vienna, Austria

## ARTICLE INFO

### Article history:

Received 18 October 2016

Received in revised form 17 February 2017

Accepted 23 February 2017

Available online 27 February 2017

### Keywords:

Analogue modelling

Sub-thrust basin inversion

Reactivation

Vertical load

Strain-softening

## ABSTRACT

This work simulates the inversion and incorporation of sub-thrust segmented half-graben basins into tectonic wedges by means of sandbox analogue models. Segmented half-graben basins - striking at 90°, 45° and 15° to the extension direction - were created first, and then shortened using different angles for the basal detachment and topographic slope. A shallow viscous polymer layer located above the half-graben basin was included in one of the models. The experiments were analysed using time-lapse photography, topography laser scans and image-based 3D voxels. The results indicate a deformation sequence characterised by layer-parallel compaction, fault reactivation, thrust propagation and related folding. Fault reactivation was associated with the layer-parallel compaction accomplished by slip along the basal detachment, prior to and in between pulses of thrusting. Results reveal the fundamental control imposed by the vertical load of the tectonic wedge and its integrated strength profile in the inversion of sub-thrust basins. Results are compared to the Alpine-Carpathian fold-and-thrust belt.

© 2017 Elsevier B.V. All rights reserved.

## 1. Introduction

Extensional fault systems in rifted continental margins are systematically segmented by the occurrence of soft- and hard-linked transfer fault systems (e.g., Gibbs, 1984; Morley et al., 1990; Gawthorpe and Hurst, 1993). This segmentation arises from the interaction of fault growth processes with pre-existing crustal features that become reactivated upon rifting (e.g., Bartholomew et al., 1993; Faulds and Varga, 1998; Morley, 2010; Fossen et al., 2016). In this sense, structural inheritance may also play an important role during subsequent shortening stages. In collisional foredeeps, rifted continental margins are buried by foreland sedimentary systems and, ultimately, become overridden by advancing fold-and-thrust belts. With ongoing collision, compressive stresses can be transmitted into the foreland plate, causing the positive inversion of these deep-seated sub-thrust basins (Fig. 1) under compressional and/or transpressional stress regimes (e.g., Ziegler et al., 2001). Studies on fold-and-thrust belts such as the European Alpine system (e.g., Gillcrist et al., 1987; Williams et al., 1989; Huyghe and Mugnier, 1995; Muñoz, 2002; Mencos et al., 2015), the High Atlas (e.g., El Harfi et al., 2006), the Apennines (e.g., Scisciani, 2009), the Andes (e.g., Carrera and Muñoz, 2013) as well as numerical modelling

works (e.g., Buiter et al., 2009; Nilfouroushan et al., 2013; Erdős et al., 2014), have illustrated that inversion of sedimentary basins is largely controlled by the inherited lithospheric architecture, including: (1) the physical properties of pre-existing fault systems and their orientation in relation to stress trajectories; (2) basin geometry and the physical properties of the stratigraphic infill; (3) basement type/s; (4) thermal history; (5) the integrated lithospheric strength profile and its variations through time (e.g., Ziegler et al., 2001). All these factors can be included in the concept of inheritance (e.g., Holdsworth et al., 2001).

The study presented here has been motivated by the recent interpretation of sub-thrust positive inversion structures below the Alpine-Carpathian fold-and-thrust belt (e.g., Granado et al., 2016; Fig. 2). The Höflein high (Fig. 3) is one of the largest hydrocarbon fields in the area and corresponds to a structurally complex basement high, poorly covered by available 3D seismic data. Similar sub-thrust structures are known to host large hydrocarbon reserves in other fold-and-thrust belts, but their 3D structure and kinematics also remain poorly constrained due to deep burial and limited seismic resolution (e.g., Zimmer et al., 1996; Shiner et al., 2004; D'Adda et al., 2017). By controlling the modelling parameters, sandbox analogue models can provide structurally balanced and scaled solutions aiding in the interpretation process (e.g., Koopman et al., 1987; McClay, 1989, 1995, 1996; Buchanan and McClay, 1991, 1992; Sassi et al., 1993; Vially et al., 1994; Eisenstadt and Withjack, 1995; Storti and McClay, 1995; Brun and Nalpas, 1996; Roure and Colletta, 1996; Dubois et al., 2002;

\* Corresponding author at: Institut de Recerca Geomodels, Universitat de Barcelona, Martí i Franquès s/n, 08028 Barcelona, Spain.

E-mail address: [pablomartinez\\_granado@ub.edu](mailto:pablomartinez_granado@ub.edu) (P. Granado).

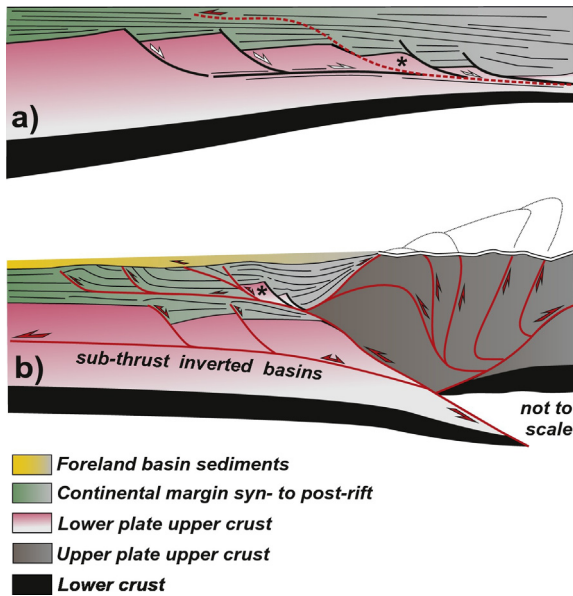


Fig. 1. a) Continental margin. b) Orogenic belt displaying extensional basins imbricated on a fold-and-thrust belt, and sub-thrust inverted basins.

Yamada and McClay, 2004; Eisenstadt and Sims, 2005; Panien et al., 2005; Del Ventisette et al., 2006; Bonini, 2007; Bonini et al., 2012; Di Domenica et al., 2014). In this work, the impact of the vertical load and the strength profile of tectonic wedges on the inversion of structurally segmented sub-thrust basins were investigated by means of sandbox models. For this matter, the experimental approach included the deformation of tectonic wedges using different basal detachment dips and topographic slopes (i.e.,  $\beta$  and  $\alpha$  angle, respectively) over a frictional basal detachment.

The analysis of the experimental results was focused on two models sharing the same tectonic wedge configuration, one with a shallow viscous detachment above the half-graben basin and one without it, aimed to represent end members of structural coupling. Insights into the geometry, the kinematics and the timing of basin inversion vs. thrust propagation were obtained. To aid in the interpretation of the experimental results, image-based 3D voxel reconstructions (see Dooley et al., 2009) were also carried out. Using longitudinal serial cross-sections as seeds, the technique allows correlating along-strike both the extensional and compressional architectures of the models by means of mutually-orthogonal virtual depth-slices and inline-sections. The experimental results are presented and compared to the Höfflein high natural prototype, discussing the competing factors that may influence the role of inheritance in natural systems.

## 2. Geological framework

The Alpine-Carpathian fold-and-thrust belt is located in the transition between the Eastern Alps and the Western Carpathians (Fig. 2a) to the south of the Bohemian Massif (Fig. 2b). Beneath the fold-and-thrust belt, the former Middle Jurassic to Early Cretaceous rifted margin of the European plate is represented by the Lower Austria Mesozoic Basin (e.g., Wessely, 1987). Although structurally segmented, the basement fault array of the basin is dominantly NE-SW-striking and steeply SE-dipping (Fig. 2c). The basement fault system originated during the late stages of the Variscan cycle (e.g., Wagner, 1998), and since then, became reactivated in several episodes (e.g., Granado et al., 2016). Convergence between Adria and Europe led to the formation of an accretionary prism as the oceanic lithosphere of the European plate was subducted beneath the Adriatic plate. Upon continental collision, the Alpine-Carpathian fold-and-thrust belt developed from late Eocene to early Miocene by the N- to NW-directed overthrusting of the Adriatic plate

and the accretion of the Alpine Tethys continental margin sequences onto the European platform (e.g., Decker and Peresson, 1996; Schmid et al., 2004; Beidinger and Decker, 2014). In NE Austria, the Lower Austria Mesozoic Basin and its crystalline basement were overthrust by this thin-skinned fold-and-thrust belt along the shale sequences of the uppermost post-rift and lowermost foreland sediments (e.g., Wagner, 1998; Beidinger and Decker, 2014). Thin-skinned thrusting was followed by the selective reactivation of the basement faults and the formation of new basement-involved thrusts between late early Miocene to earliest middle Miocene. The basement extensional faults and the basement-involved thrusts broadly share the same orientation as constrained by the seismic interpretation and 3D structural modelling carried out (Fig. 2c). The basement-involved shortening was responsible for the formation of the Höfflein high and other inversion structures in the sub-thrust and the foreland (e.g., Granado et al., 2016; Fig. 2d).

The Höfflein high (Fig. 3a) corresponds to the elevated footwall of the Höfflein fault, which is constituted by three segments of distinct mean orientations (Fig. 3c): a Segment 1, dipping  $70^\circ$  towards  $114^\circ$  (i.e., NNE-striking); a Segment 2, dipping  $76^\circ$  towards  $175^\circ$  (i.e., E-W-striking); and a Segment 3, dipping  $74^\circ$  towards  $136^\circ$  (i.e., NE-SW-striking). Based on these orientations and the NW-directed direction of shortening in early Miocene (Beidinger and Decker, 2014), these three fault segments would have been at  $15^\circ$ ,  $45^\circ$  and  $90^\circ$  to the shortening direction, respectively (Fig. 3). Interpretation from 3D depth-converted seismic data and well intersections has shown that the Alpine Basal Thrust is folded above the Höfflein high. These observations indicate that the uplift was produced after thin-skinned thrusting and by the development of deeper, basement-involved thrusts. Based on this, Granado et al. (2016) interpreted the Höfflein high as a harpoon structure (i.e., Williams et al., 1989) constituted by a mildly inverted extensional fault and an imbricate fan of basement-involved footwall shortcut thrusts. From middle Miocene onwards, lateral extrusion of the Eastern Alps towards the Carpathian embayment led to the collapse and burial of the orogenic wedge beneath the Pannonian basins system (Fig. 2a, d). This burial affected largely the fold-and-thrust belt and included parts of its foreland and wedge-top basin (e.g., Ratschbacher et al., 1991; Tomek and Hall, 1993; Fodor, 1995; Decker and Peresson, 1996; Huisman et al., 2001; Strauss et al., 2001; Horváth et al., 2006; Hölzel et al., 2010).

## 3. Analogue modelling

### 3.1. Rationale

Despite the large amount of analogue modelling works on basin inversion to date, few have addressed the inversion of continental margins during the development of tectonic wedges (e.g., Bonnet et al., 2007). A non-cylindrical (i.e., 3D) approach was used for the experimental programme presented here. In such a way, and for the first time, the inversion and imbrication of segmented half-graben basins beneath and ahead of developing fold-and-thrust belts was simulated. Segmented half-graben basins were modelled first, and then shortened using different angles for the basal detachment and topographic slope. A shallow viscous polymer layer, located above the half-graben basin, was included in one of the models (Table 1). The methodology, materials' properties, scaling and the combination of analytical techniques used in this study are described in the following sections.

### 3.2. Experimental methodology

#### 3.2.1. Set-up

The experimental programme was carried out at the *Geomodels Analogue Modeling Laboratory* of the University of Barcelona. A similar set up to that described by Brun and Nalpas (1996), Smit et al. (2003), Schreurs et al. (2006), Graveleau et al. (2012) or Bonini et al. (2012) for physical

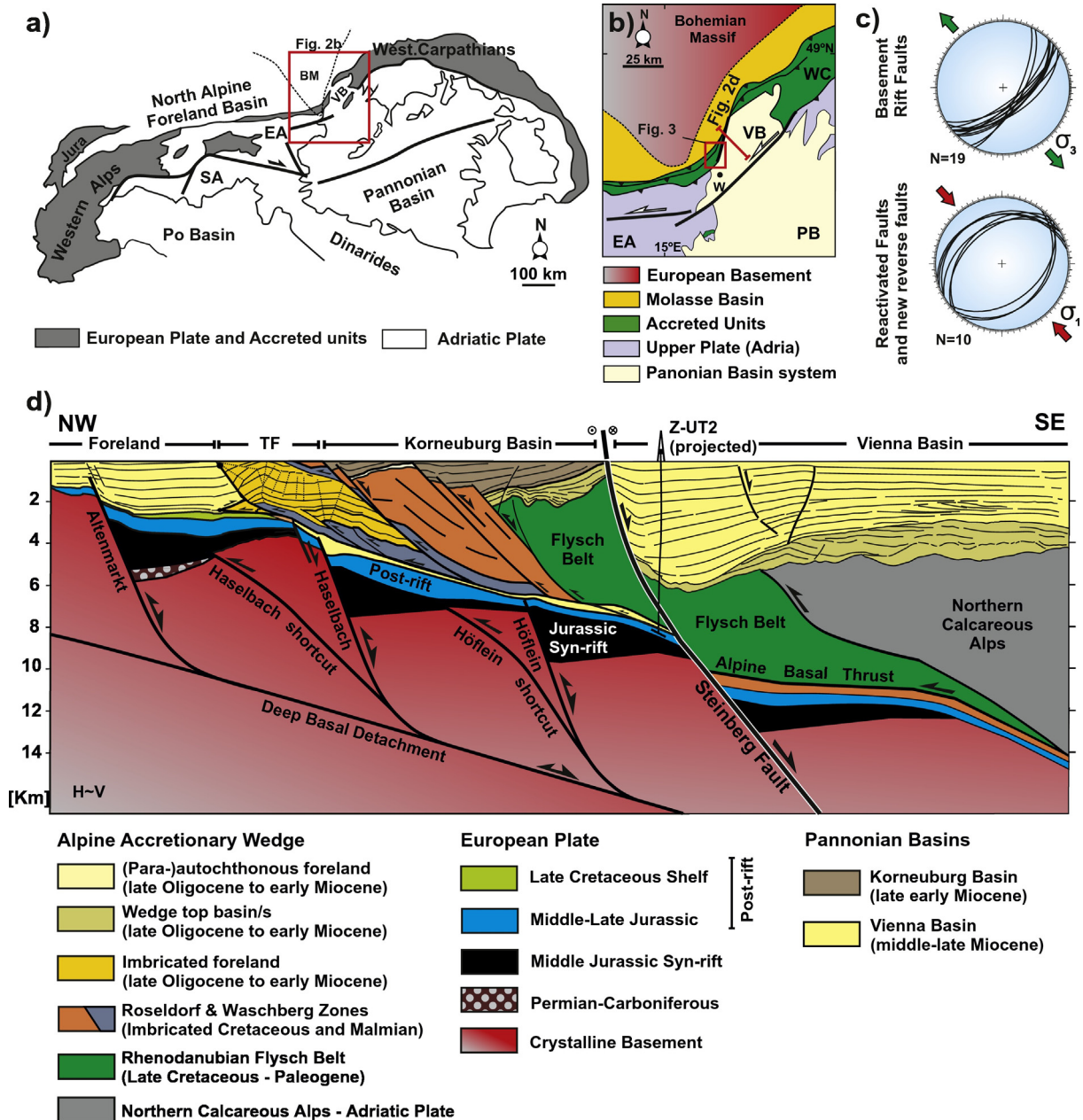


**Fig. 2.** Geological setting. a) Sketch of the Alpine-Carpathian-Pannonian tectonic framework (modified from Decker and Peresson, 1996). b) Simplified tectonic map of the Alpine-Carpathian Junction. c) Mean orientations of the Lower Austria Mesozoic Basin basement fault array. d) NW-SE-striking regional cross-section along the Alpine-Carpathian foreland, fold-and-thrust belt and the Pannonian basins (Korneuburg and Vienna basins). Modified from Zimmer et al. (1996), Beidinger and Decker (2014) and Granado et al. (2016). BM: Bohemian Massif; EA: Eastern Alps; PB: Pannonian Basin; PM: Para-Autochthonous Molasse; SA: Southern Alps; VB: Vienna Basin; W: Vienna; WC: Western Carpathians.

analogue experiments of brittle and brittle-ductile systems was used. The experimental rig consisted on two glass-sided walls, a fixed wall, and a moving backstop wall with pre-deformation dimensions of  $75 \times 50 \times 6 \text{ cm}^3$ . A strong plastic sheet was set at its base to simulate the basal detachment surface (Fig. 4). The plastic sheet was not deformed under the modelling conditions and maintained its length during the experiments. On top of the plastic sheet, a 2 mm-thick basal rigid plate with dimensions of  $45 \times 50 \text{ cm}^2$  was attached to the fixed wall (Fig. 4). This rigid plate was built with a non-rectilinear boundary inspired on the Höflein fault but aimed at providing a 3D component to the segmented extensional fault system. The rigid plate consisted on two segments oblique to the extension and shortening directions (i.e., one at  $15^\circ$  and another at  $45^\circ$ , such as segments 1 and 2 of the Höflein fault, respectively); the third fault segment perpendicular to both directions of deformation would correspond to the fault segment 3 (compare

Figs. 3 and 4). Using a large rigid footwall block, or a rotating mechanical domino set up (Wernicke and Burchfield, 1982; McClay, 1989, 1995) was discarded to minimise the forced reactivation, and to allow for the 'free' deformation of the sandpack and the development of footwall shortcut thrusts by slip along the basal detachment (e.g., Panien et al., 2005; Bonini et al., 2012; Di Domenica et al., 2014).

### 3.2.2. Analogue materials and scaling

The models were constructed using modelling materials suitable to carry out simulations of upper crustal deformation (see Davy and Cobbold, 1991; Weijermars and Schmeling, 1986; Schellart, 2000; Lohrmann et al., 2003; Adam et al., 2005; Dell'Ertole and Schellart, 2013; Schellart and Strak, 2016). An extension rate of 1 cm/h was applied to all models given that the rheology of dry quartz sand is not strain rate dependent and that no proper estimates for the rate of

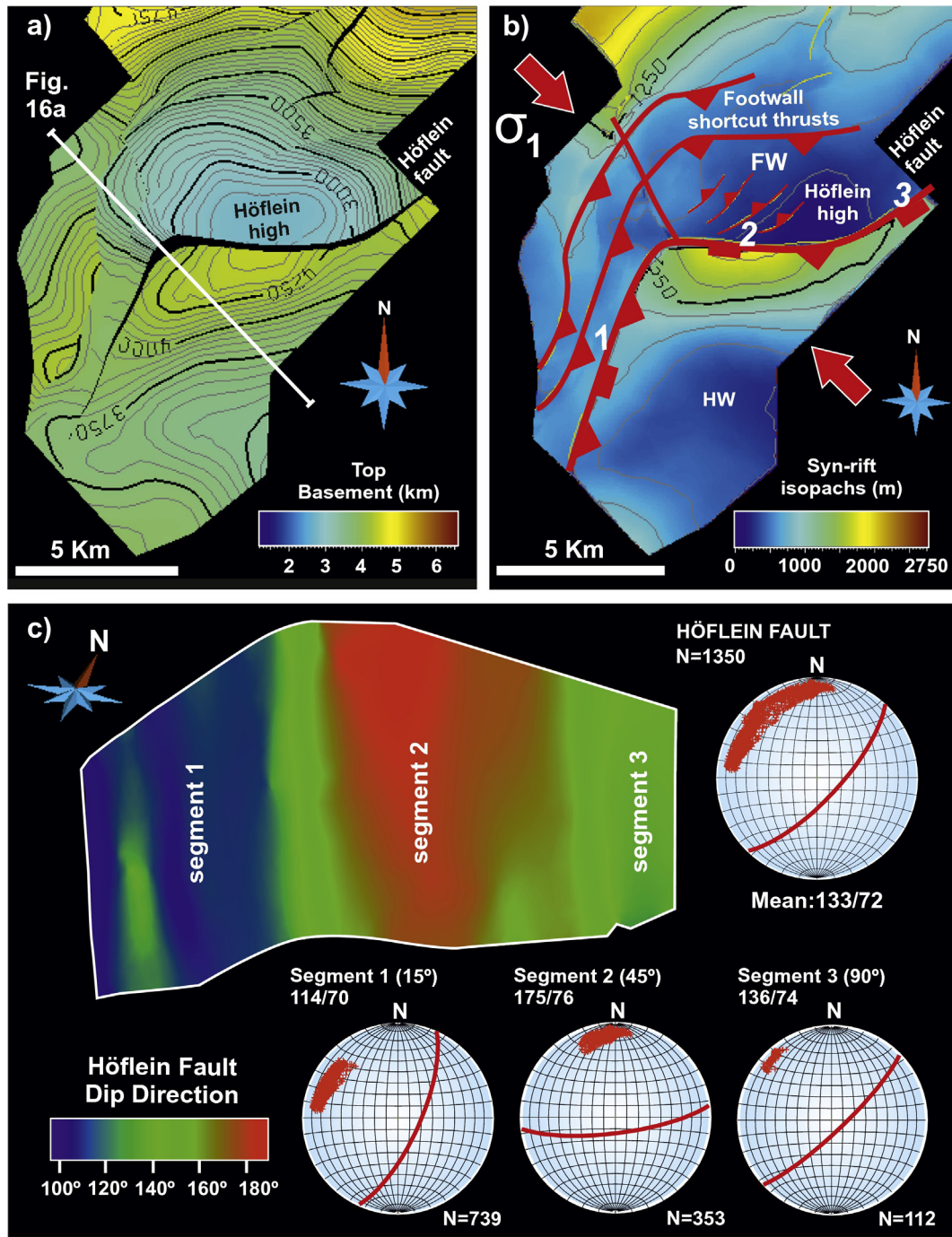


**Fig. 3.** 3D structure of the Höflein high and related fault segments. a) Top Basement structure map of the Höflein high. b) Syn-rift true stratigraphic thickness map of the Höflein half-graben. Numbers 1, 2 and 3 refer to the three fault segments individuated for the Höflein fault. c) Mean orientation of the Höflein fault and its three fault segments. See text for further details.

Jurassic rifting at the Lower Austria Mesozoic Basin are available. Based on the structural decoupling observed between thin-skinned thrust systems and sub-thrust basins, a strain-rate dependent polymer was used

in one of the experiments carried out (see Table 1 and further explanations in the following). A 1.5 cm/h velocity of shortening was chosen after proper scaling using the polymer characteristics and the thrust

**Table 1**  
Main parameters of the experimental programme.

	Basal detachment	Dip ( $\beta$ )	Shallow detachment	Topography slope ( $\alpha$ )	Wedge ( $\alpha + \beta$ )	Total extension	Extension rate	Total shortening	Shortening rate
Model 1	Frictional	0°	–	0°	–	5 cm	1 cm/h	–	–
Model 2	Frictional	0°	–	0°	0°	5 cm	1 cm/h	6 cm	1.5 cm/h
Model 3	Frictional	3°	–	32°	35°	5 cm	1 cm/h	15 cm	1.5 cm/h
Model 4	Frictional	3°	–	3°	6°	5 cm	1 cm/h	15 cm	1.5 cm/h
Model 5	Frictional	3°	–	0°	3°	5 cm	1 cm/h	15 cm	1.5 cm/h
Model 6	Frictional	3°	Viscous	0°	3°	5 cm	1 cm/h	15 cm	1.5 cm/h

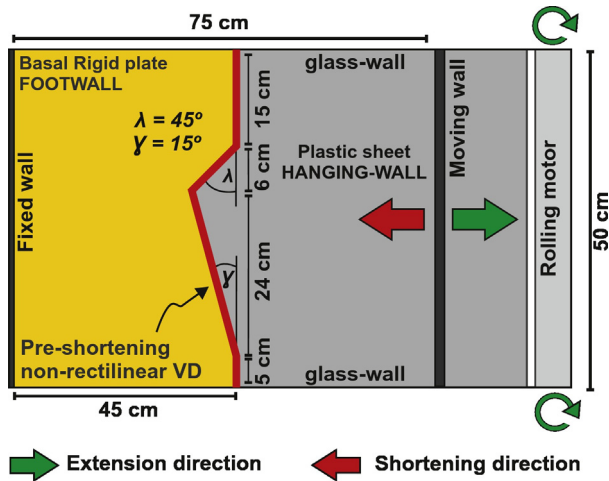


Fig. 4. Experimental set up. a) Top-view sketch of the experimental setup with the terminology used in this article. Note the 3 different segments of the rigid basal plate at 90°, 45° and 15° to the extension and shortening directions. Compare with Fig. 3c.

velocities estimated for the area by Beidinger and Decker (2014). The properties of the materials used and the scaling of the experimental programme are summarised on Table 2.

Dry well-sorted quartz sand with an average grain size of 250  $\mu\text{m}$ , a mean coefficient of friction ( $\varphi$ ) of 0.6, and an average angle of internal friction ( $\phi$ ) of  $\sim 34^\circ$ , a bulk density of 1600  $\text{kg}/\text{m}^3$  and cohesive strength of around 55 Pascals was used. As demonstrated by Lohrmann et al. (2003) and Adam et al. (2005), sand displays an elastic/frictional plastic behaviour with transient strain hardening prior to transition to stable sliding. According to their works, the behaviour of dry quartz sand departs from the classically accepted Mohr-Coulomb rheology (e.g., Hubbert, 1951), but still remains a good mechanical analogue for modelling the brittle behaviour of upper crustal rocks. In particular, sand is considered to be a good analogue material to model settings where the frictional reactivation of faults happens to be mild (e.g., Eisenstadt and Sims, 2005).

The polymer used to replicate the shallow detachment of the thin-skinned fold-and-thrust belt was Rhodosil GUM FB from Bluestar Silicones, a transparent high-viscosity polydimethylsiloxane (see Dell'Ertole and Schellart, 2013). At the low velocities of deformation used in the analogue models presented in this study (Table 1), this polymer behaves as a nearly-Newtonian fluid with low yield strength and a stress exponent  $n$  of  $\sim 1$  (e.g., Davy and Cobbold, 1991; Weijermars and Schmeling, 1986; Dell'Ertole and Schellart, 2013). This rheological behaviour is appropriate to simulate the natural deformation of salt or overpressured shale formations in upper crustal settings (e.g., Weijermars et al., 1993; Couzens-Schultz et al., 2003; Smit et al., 2003; Santolaria et al., 2015; Schellart and Strak, 2016). In comparison with the polymer detachment, the basal detachment constituted by the plastic sheet can be considered frictional as indicated by the dominant breaking-forward sequence of thrusting and the lack of any significant

back-thrusting observed (e.g., Couzens-Schultz et al., 2003; Smit et al., 2003; Gravelleau et al., 2012).

### 3.2.3. Procedure

A pre-deformational sandpack was built by pouring layers of even thickness of white-, blue- and black-coloured sand over the basal rigid plate and the plastic sheet. Sand layers of 0.4 cm thickness were laid to facilitate tracking of deformation (Fig. 5a). Subsequently, all models were subjected to 5 cm of extension parallel to the glass-sided walls of the rig at a constant rate of 1 cm/h. Deformation was carried out by a computer-controlled rolling engine that pulled the plastic sheet away from the fixed basal plate. This forced an asymmetric velocity discontinuity at the base of the sandpack and the consequent development of a half-graben (Fig. 5b). At the same time, the moving backstop wall was pulled by a worm screw attached as well to a computer-controlled engine. Both engines worked synchronously at the same rate to avoid differential shortening or extension of the sandpack. The accommodation space created during extension was filled with alternating layers of poured red-, white- and black-coloured sand simulating *syn*-rift deposits. Extension was halted every 30 min to add each new layer of *syn*-rift sand. The *syn*-rift sand was only poured inside the developing half-graben basin to fill the accommodation space created during each step of extension. For this, the top of the undeformed pre-rift layers was used as a regional reference of elevation. These steps were repeated until a total of 5 cm of extension were completed. Following extension, all models were covered with an even layer of orange-coloured sand to simulate a post-rift cover (Fig. 5b). This post-rift layer was used as a regional datum of elevation to assess the degree of shortening and uplift of the extensional basins during the subsequent phases of deformation.

For the shortening phase the rolling engine was locked and deformation was applied exclusively by pushing the backstop wall towards the 'undeformed foreland' at a constant velocity of 1.5 cm/h. For shortening, the first shortening model (i.e., Model 2) was kept horizontal whereas for the rest of the shortening experiments (i.e., Models 3 to 6) the deformation rig was tilted  $3^\circ$  towards the backstop moving wall (Fig. 5). In such a way, a series of distinct hinterland-thickening wedges were built by pouring brown and white layers of sand. The parameters changed for the modelling were: the dip of the basal detachment ( $\beta$ ), the topographic slope ( $\alpha$ ), the wedge angle ( $\alpha + \beta$ ), and the presence or absence of a shallow viscous detachment in an equivalent post-rift position. The models carried out and their characteristics are summarised on Table 1 and in Fig. 5. Although erosion and sedimentation are known to have a significant impact on the kinematics of tectonic wedges (e.g., Storti and McClay, 1995; Bonnet et al., 2007; Malavieille, 2010; Gravelleau et al., 2012), these were omitted for the sake of simplicity.

### 3.2.4. Analysis

In order to keep record of the experiments during extension and shortening, time-lapse high-resolution digital photographs were taken from the lateral sides of the model, from an oblique point of view and from the top of the model at 15 s intervals. Videos from these time-lapse photos were generated for kinematic analysis of deformation (see online Supplementary material). A white-light scanner was also used to record the topographical evolution of the models. During extension, these scans were carried out after stopping the deformation rig and before adding each corresponding *syn*-rift layer (i.e., after each 0.5 cm increments of extension). During shortening, scans were made after stopping the rig and for each 3 cm deformation increments. At the end of each experiment, the models were preserved and then longitudinally sectioned at 3 mm spacing. A 4 cm wide section along each side of the experiments was discarded to remove any border effects. High-resolution photographs of the longitudinal cross-sections were then imported as seeds to generate 3D voxel models. Image-processing software was used to generate mutually orthogonal crosslines, inlines

Table 2  
Scaling parameters.

Parameter	Experiment	Nature	Model/nature
Length (L)	1 cm	1 km	$1.10^{-5}$
Gravity (g)	9.81 $\text{m}/\text{s}^2$	9.81 $\text{m}/\text{s}^2$	1
Density ( $\rho$ )	1.6 $\text{g}/\text{cm}^3$	2.6 $\text{g}/\text{cm}^3$	0.61
<i>Dry quartz sand</i>			
Density ( $\rho$ )	0.97 $\text{g}/\text{cm}^3$	2.2 $\text{g}/\text{cm}^3$	0.44
<i>Polymer</i>			
Viscosity ( $\eta$ )	$1.18 \times 10^4$ Pa·s	$5 \times 10^{18}$ Pa·s	$2.3 \times 10^{-15}$
Time (t)	1 h	258,270 yrs	$4.42 \times 10^{-10}$
Velocity (V)	1.5 cm/h	5 mm/yrs	$2.26 \times 10^4$

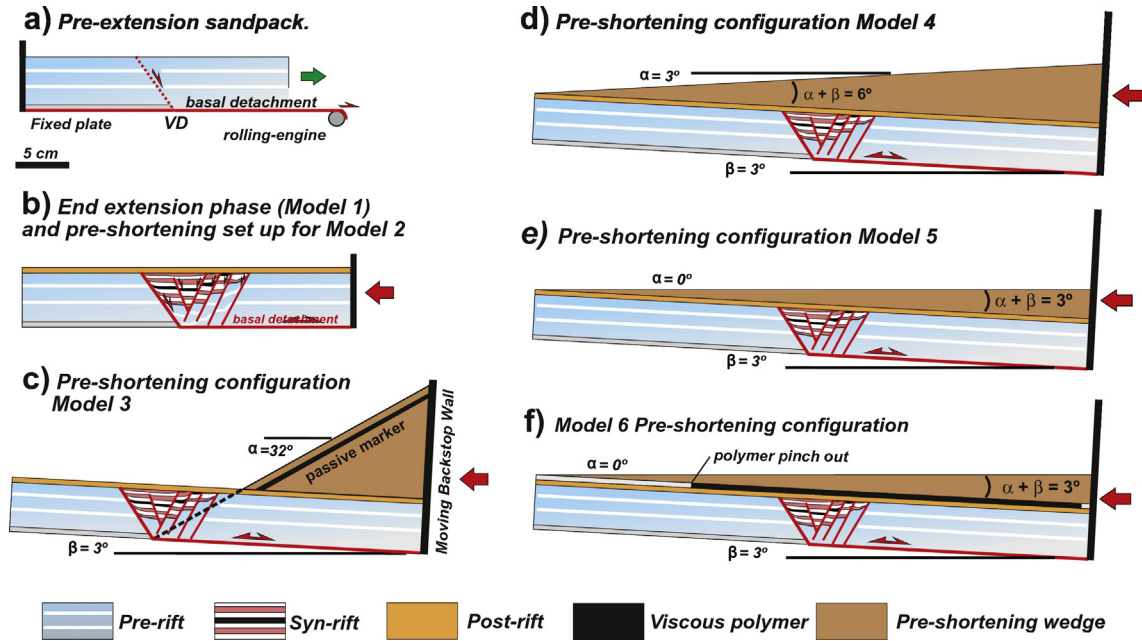


**Fig. 5.** Summary of the sandbox models set ups carried out in this study. a) Baseline extensional model set up previous to extension. b) Model 1 after 5 cm of extension. The results of Model 1 are also the pre-shortening configuration for shortening Model 2. c) Pre-shortening configuration for Model 3. d) Pre-shortening configuration for Model 4. e) Pre-shortening configuration for Model 5. f) Pre-shortening configuration for Model 6. See Table 1 for further details.

and depth-slices that allowed for better visualisation and interpretation of the experimental results.

#### 4. Experimental results

##### 4.1. Baseline extensional model results (Model 1)

A segmented half-graben basin was developed during the extensional deformation stage of each model. Time-lapse photography (see online supplementary material) has shown that during the earliest stages of extension a master border fault was developed above the velocity discontinuity. An early fault scarp developed above the segments at 90° and 15° to extension, whereas a monocline dipping into the half-graben was developed at the fault segment trending at 45° to extension (Fig. 6a). With ongoing extension, the monocline became breached, and the upward-propagating fault segments were linked along strike (Fig. 6b). Secondary faults, including antithetic and, to a lesser extent synthetic faults, grew as initially sinuous and isolated fault segments, trending parallel to the bisector of the normal to the extension direction and the corresponding velocity discontinuity segment. This is well illustrated by the synthetic fault that breached the monocline developed at the 45° segment. Initially isolated fault segments were developed on those fault segments at 90° and 15° to the extension direction, linking laterally with other isolated fault segments to produce less sinuous, longer strike faults (Fig. 6b). Overall, these faults grew migrating laterally from the 15° and 90° segments towards the 45° fault segment located in the central part of the sandbox model. The formation of additional antithetic faults always took place into the interior of the developing half-graben basin. As extension accumulated, the formerly developed antithetic fault systems progressively took less displacement and became abandoned. At the 45° segment, extensional relay ramps were generated in all the models (Fig. 6b). With continued extension, these relay ramps were eventually breached to form longer strike faults. Oppositely, the master border fault displayed a continuous activity during the extensional phase in all models, developing accommodation space immediately above the velocity discontinuity. This kinematic evolution was observed for all the models carried out in this study.

The internal 3D architecture of the segmented half-graben basin was additionally constrained by means of serial cross sections (Fig. 6c–e)

and 3D image-based voxels (Fig. 7). Serial cross-sections have shown differences in regards of the number of faults and their spacing along strike (i.e., fault density): a total of 4 narrowly-spaced antithetic faults were developed at the 90° and 15° segments, whereas only 3 widely-spaced antithetic faults were developed at the central 45° segment. A synthetic fault was also developed at the central 45° segment and was responsible for the formation of a rider block (Fig. 6d). The developed antithetic faults were planar and showed similar cut-off angles at the 90° and 15° segments. Conversely, the antithetic faults developed at the 45° segment display a steepening, concave upwards geometry. The plan view geometry of the extensional basin is shown by a depth-slice (Fig. 7a) as a ribbon of syn-rift layers (i.e., red-, white- and black-coloured sand). These layers follow the shape of the basal rigid plate (see Fig. 4 for comparison with the deformation rig set up). Faults were revealed as thin linear features of coloured sand and correspond to the dragged sand layers produced by extension along discrete fault zones. The breached relays ramps and the breached monocline at the 45° fault segment are shown as patches of red- and white-coloured sand on the depth-slice (Fig. 7a). Three virtual inline sections (i.e., sections normal to the direction of extension; Fig. 7b–d) were generated from the 3D voxel and have shown the along-strike structural change of the basin from the footwall to the hanging-wall (i.e., sections from I–I' to III–III'). For those inline-sections striking at low angles to the faults, the shallowly-dipping fault traces show the apparent dips of the extensional faults (Fig. 7b–d).

##### 4.2. Shortening results

###### 4.2.1. Shortening Model 2

This model consisted in the simulation of the inversion of a shallowly buried segmented half-graben basin by shortening the sandpack without any previous topography (i.e.,  $\alpha = 0^\circ$ ) along a horizontal detachment (i.e.,  $\beta = 0^\circ$ ). The pre-shortening configuration for Model 2 is shown in Fig. 5b. This set up allowed establishing a baseline model for comparison with the following ones. The total amount of shortening was 6 cm (i.e., slightly more than the amount of extension) and resulted in the formation of a pop-up anticline (Fig. 8) with no preferred structural vergence. The anticline was affected by surface-breaching faults which correspond to reactivated extensional faults (Fig. 8a), as well as

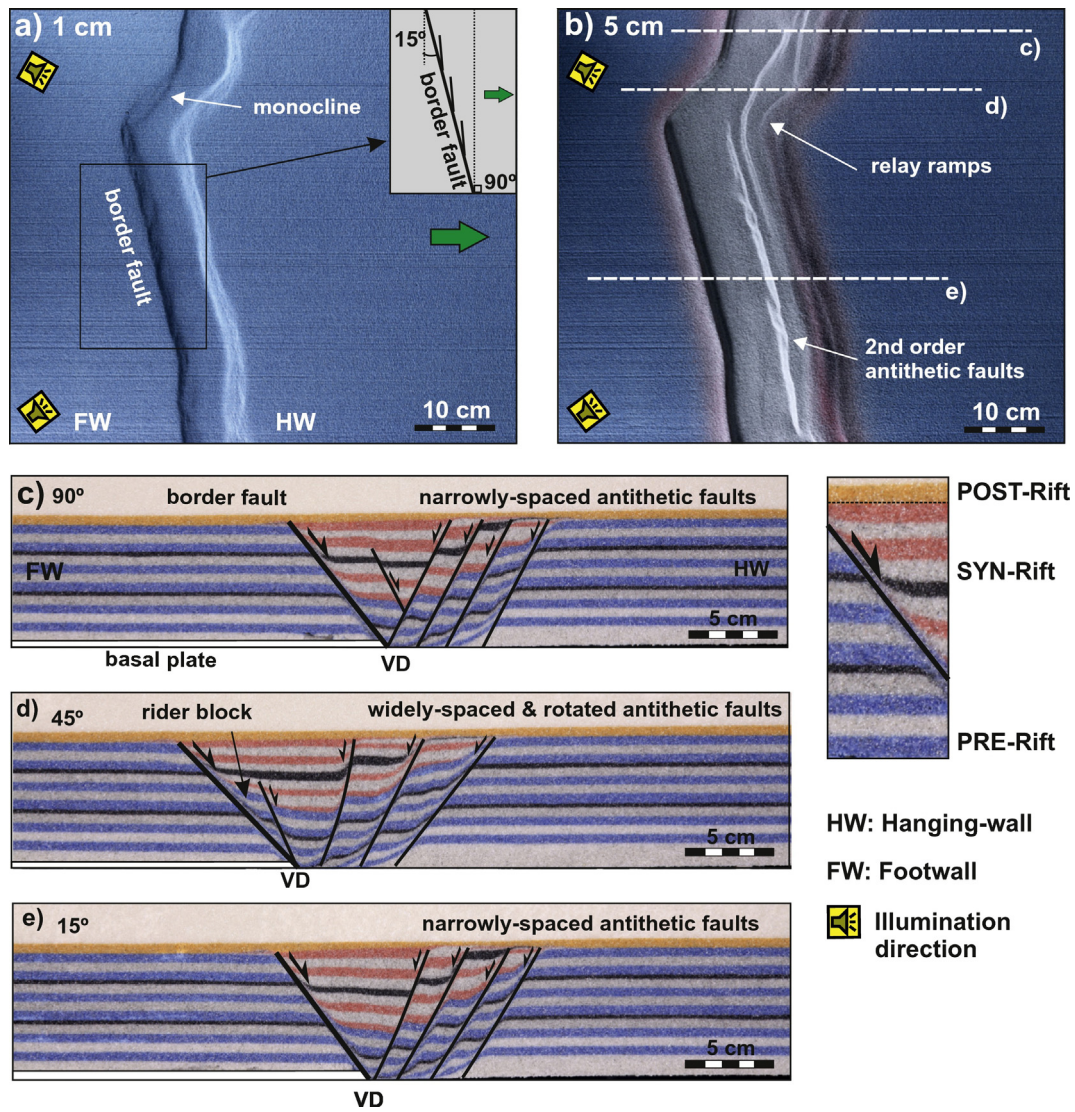


**Fig. 6.** Summary of results for baseline extension Model 1. Illumination is from the left. Shadowed areas are surface-breaching faults dipping to the right and illuminated areas are surface-breaching faults dipping to the left. a) Top view after 1 cm of extension. b) Top view after 5 cm of extension. c) Cross-section along the 90° segment. d) Cross-section along the 45° segment. e) Cross-section along the 15° segment. FW: Footwall. HW: Hanging-wall. VD: Velocity discontinuity.

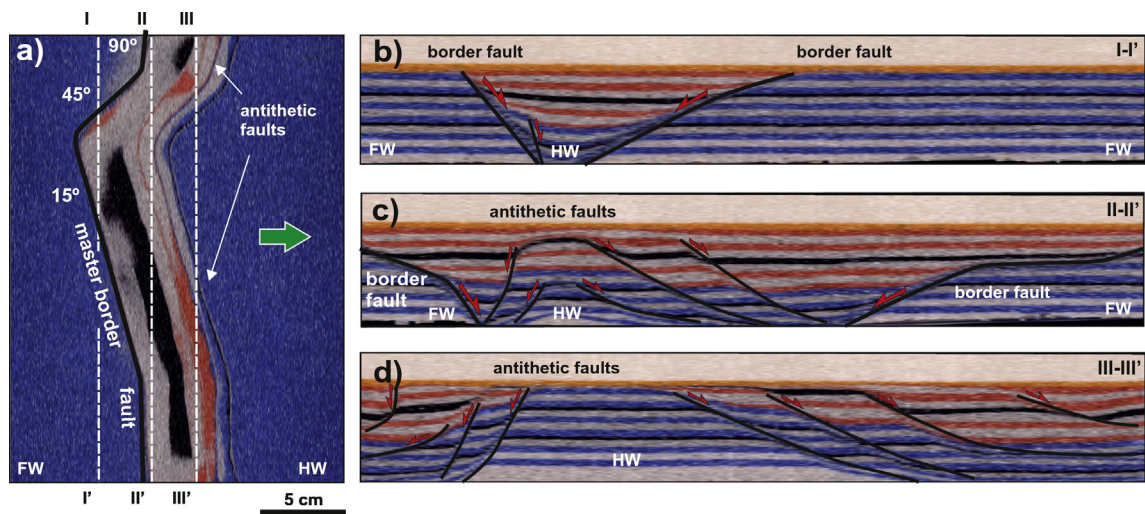


**Fig. 7.** Virtual sections extracted from the 3D voxel of Model 1. a) Depth-slice showing the top view geometry of the half-graben basin. b) Virtual inline passing by the tip of the extensional basin. c) Virtual inline passing along the central parts of the half-graben basin. d) Virtual inline passing by the 90° and the 15° segments. Shallow dips of the extensional faults are apparent dips. FW: Footwall. HW: Hanging-wall.

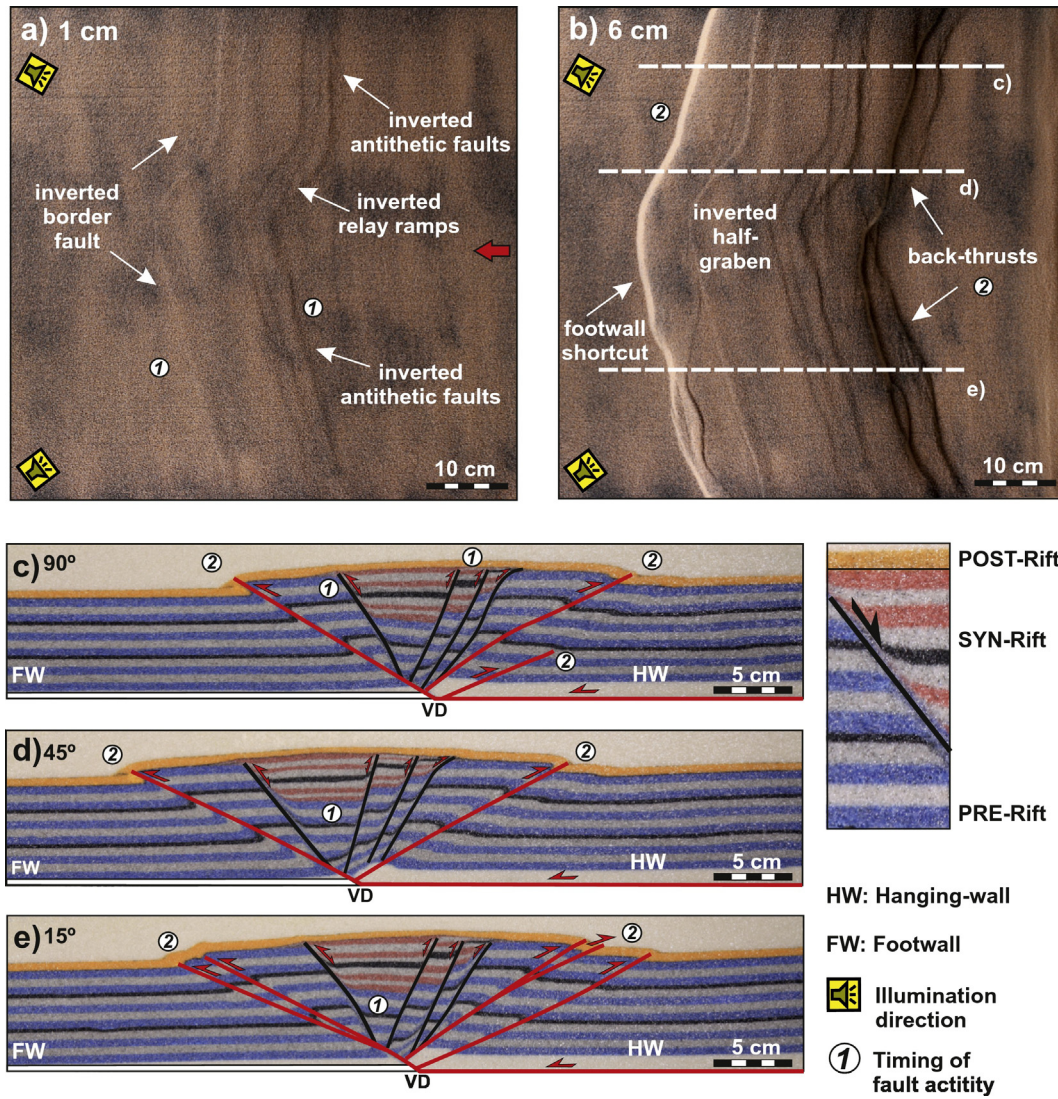


**Fig. 8.** Summary of results for Model 2. Illumination is from the left. Shadowed areas are surface-breaching faults dipping to the left, whereas illuminated zones are surface-breaching faults dipping to the right. a) Top view after 1 cm of shortening. b) Top view after 6 cm of shortening. c) Sliced cross-section along the 90° segment. d) Sliced cross-section along the 45° segment. e) Sliced cross-section along the 15° segment. Numbers indicate the relative timing of fault activity and basin inversion. FW: Footwall. HW: Hanging-wall.

two forward directed thrusts and two back-thrusts (Fig. 8a, b). On plan view, the developing pop-up anticline and the trace of the emergent thrusts and back-thrusts followed the shape of the underlying rigid plate. Serial vertical sectioning of the model has shown that the thrusts and back-thrusts display a roughly linear geometry. No significant changes along strike in the structure were observed (Fig. 8c–e). These features indicate that the deformation results could have been partially controlled by the initial boundary conditions of the model.

Time-lapse photography was used to constrain the sequence of deformation (see online supplementary material). During the earliest stages of shortening, the moving backstop wall generated sliding along the basal horizontal detachment, producing the compaction of the sandpack up to the location of the velocity discontinuity. As revealed by time-lapse photography, the first structures to form developed after a certain degree of compaction, and then, folded the surface of the sand-box model (Fig. 8a). These surface-breaching structures are shown up as lighted and shadowed linear features. These early folds mimicked the shape of the previously developed extensional fault system, including the secondary antithetic faults and the breached relay ramps. Hence, these structures are indicative for the early reactivation of the extensional fault array. As shortening continued, deformation was taken up by displacement along back-thrusts and thrusts. The back-thrusts

correspond to hanging-wall directed back-thrusts, whereas the thrusts correspond to footwall shortcut thrusts structures (e.g., McClay, 1989).

#### 4.2.2. Shortening Model 3

This model consisted on the deformation of the segmented half-graben basin located ahead of a sand wedge with a topographic slope of  $\alpha = 32^\circ$ . In contrast with the former model, the pre-shortening configuration included a hinterland-dipping basal detachment ( $\beta = 3^\circ$ ). The elevated slope was built to make it closely correspond to the internal friction threshold of the sand. The set up aimed at modelling the deformation of a near-critical wedge (i.e., in the verge of failure; see Chapple, 1978) so to test if and how the segmented half-graben was inverted and accreted to the toe of the wedge. The wedge was built onto the post-rift cover so as to pinch out in a linear fashion (i.e., at 90° to shortening direction) behind the segmented half-graben basin (Fig. 5c). The total amount of shortening was 15 cm (i.e., three times the value of extension).

Time-lapse photography allowed unravelling the sequence of deformation which is summarised on Fig. 9a and b (see online supplementary material). Similarly to Model 2, an initial phase of sand compaction took place by sliding along the basal detachment. This deformation phase was accompanied by the gentle inversion of the previously

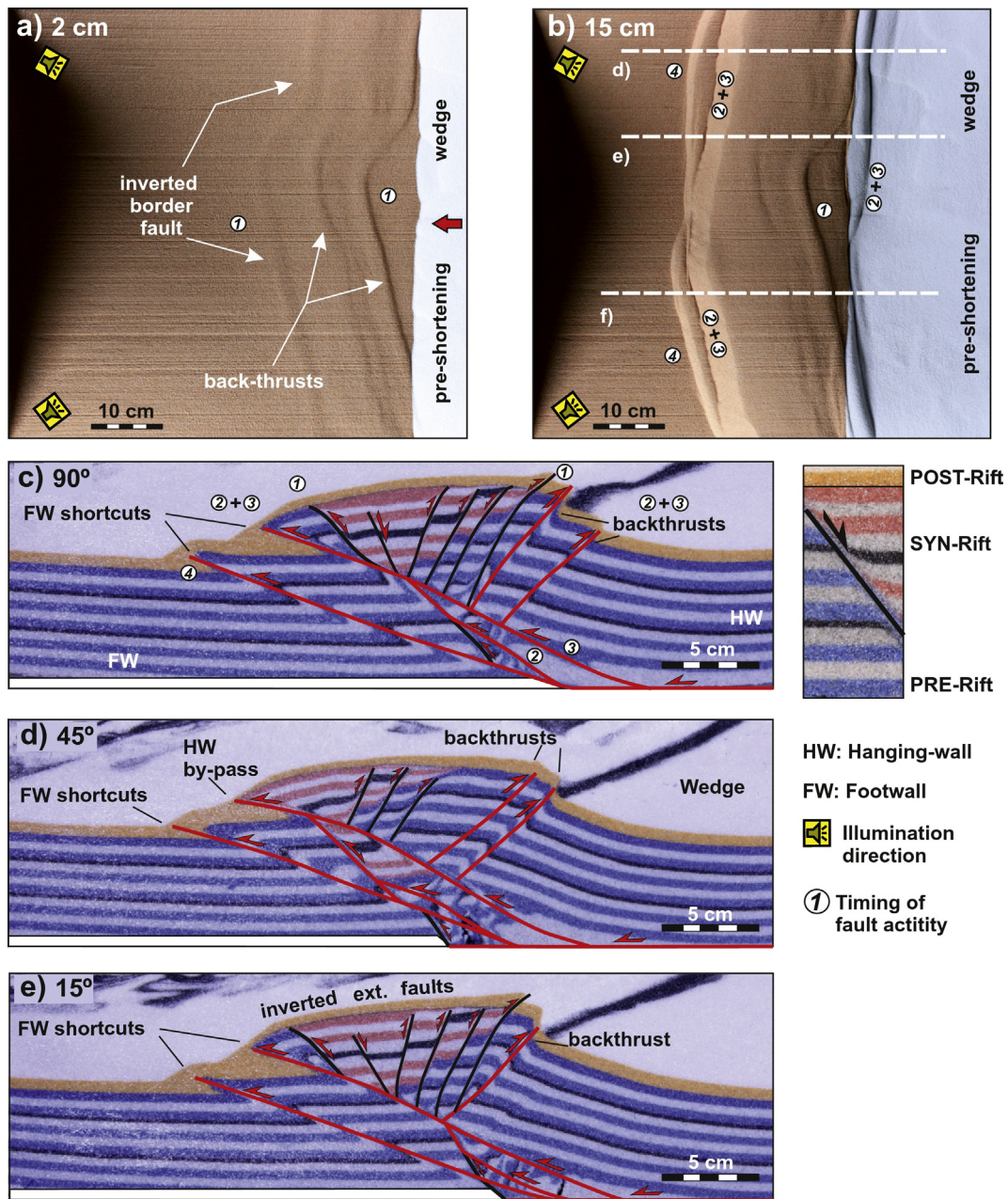


**Fig. 9.** Summary of results for Model 3. Illumination is from the left. a) Top view after 2 cm of shortening. b) End of experiment after 15 cm of shortening. c) Cross-section along the 90° segment. d) Cross-section along the 45° segment of the rigid basal plate. e) Cross-section along the 15° segment. Numbers indicate relative timing of thrust movement and basin inversion. FW: Footwall. HW: Hanging-wall.

developed extensional fault system (i.e., the master border fault and the antithetic faults) as shown by the formation of surface-breaching fault-propagation folds (Fig. 9a) above the underlying extensional fault system. Inversion was followed by emergent hanging-wall directed back-thrusts and foreland-directed thrusts which affected the pre-rift sand layers. Uplift along the foreland-directed thrusts led to the collapse of the thrust fronts by “mass-wasting”. Although the overall kinematical evolution developed broadly in sequence towards the foreland, the cross-cutting relationships shown by serial cross-sectioning and time-lapse videos (see supplementary material) revealed out-of-sequence thrusting (i.e., thrusts #2 and #3; Fig. 9c) after the reactivation of the border extensional fault. The last deformation phase was represented by the formation of an emergent footwall shortcut thrust (i.e., thrust #4; Fig. 9b, c).

Cross sections have shown significant changes along the strike of the model. Thrust #3 developed as a footwall shortcut at the 90° and 15°

fault segments, whereas it developed as a hanging-wall by-pass thrust towards the central parts of the sandbox (i.e., 45° segments). The by-pass thrust re-used the upper reaches of the border extensional fault (Fig. 9d), transporting and tilting the half-graben towards the foreland. The basin and its border fault were split in two in the central parts of the sandbox model, where it can be found in a hanging-wall and a footwall position (Fig. 9d). In the 90° and 15° segments, the inverted basin occurs imbricated on a hanging-wall position along with the master extensional fault (Fig. 9c and e).

#### 4.2.3. Shortening Model 4

This model consisted on the deformation of the segmented half-graben basin along a hinterland dipping basal detachment ( $\beta = 3^\circ$ ), with a hinterland-thickening sand wedge covering the full stretch of the model. The sand wedge was built with a 6° thickening angle and a topographic slope  $\alpha = 3^\circ$  (Fig. 5d). After 15 cm of shortening, the deformed

tectonic wedged displayed three thrust sheets with associated surface-breaching fault-propagation folds (Fig. 10). Displacement along the hinterland thrust completely overrode the segmented half-graben basin. Time-lapse photography (see online supplementary material) and topography scans have shown a sequence of deformation characterised by a first stage of sand compaction associated to slip along the hinterland-dipping basal detachment. The deformation front of this early compaction phase migrated from the hinterland towards the foreland and arrived ahead of the half-graben basin. The border antithetic fault underwent mild reactivation by back-thrusting (i.e., back-thrust #1), developing a gentle fault-propagation fold. The early deformation front can be better appreciated on the topography scan (Fig. 10b) whereas the emergent back-thrust fault-propagation fold is better shown by time-lapse photography (Fig. 10a, c). Subsequent deformation was characterised by the development of a breaking-forward thrust system (i.e., thrusts #2, #3 and #4; Fig. 10e).

The longitudinal cross-sections revealed a broadly homogeneous along-strike structure dominated by a large thrust sheet associated with thrust #2. For this reason, the cross-section at 45° is shown as a representative section for the whole model (Fig. 10e). The next thrust to develop (i.e., thrust #3) propagated forward from beneath the segmented half-graben, splitting the master extensional fault and the syn-rift wedge in two. Displacement along thrust #3 also developed a fault-propagation fold with an associated back-thrust close to the surface. In the central parts of the sandbox, an emergent thrust front was developed (i.e., thrust #4), showing a top shape parallel to the geometry of the basal plate (Fig. 10c, d). This last thrust propagated forwards in the central parts of the sandbox model but it is linked to thrust #3 towards the lateral ends of the sandbox, meaning that thrust #4 is a splay from thrust #3. Only the border antithetic fault underwent mild reactivation in this model.

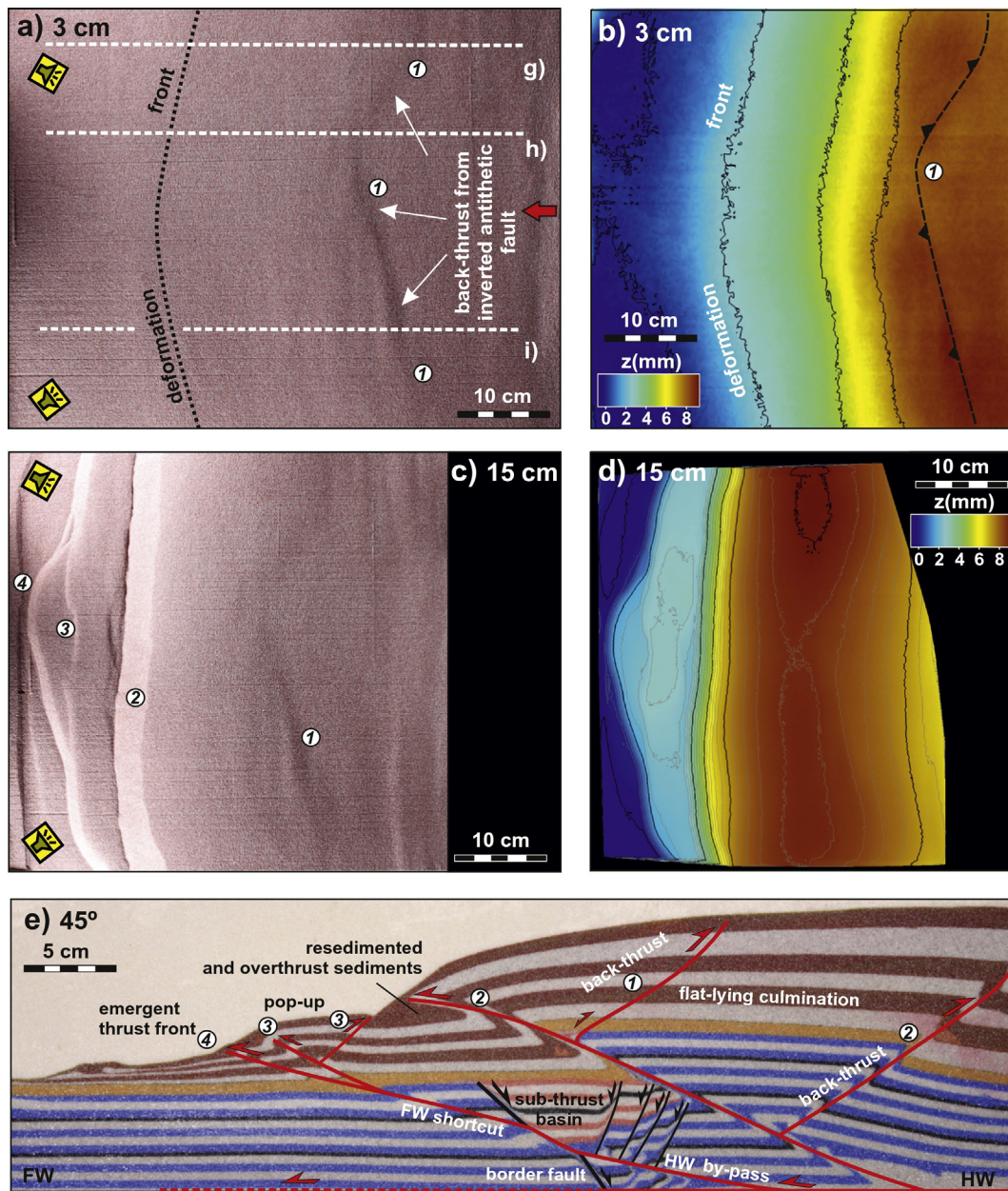


**Fig. 10.** Summary of results for Model 4. Illumination is from the left. A) Top view after 3 cm of shortening. b) Topography scan also reveals a bow-shaped deformation front developed ahead of the half-graben basin. c) Top view at the end of the experiment after 15 cm of shortening. d) Topography scan after the end of the experiment. e) Sliced cross-section along the 45° segment. Numbers indicate relative timing of thrust movement and basin inversion. FW: Footwall. HW: Hanging-wall.

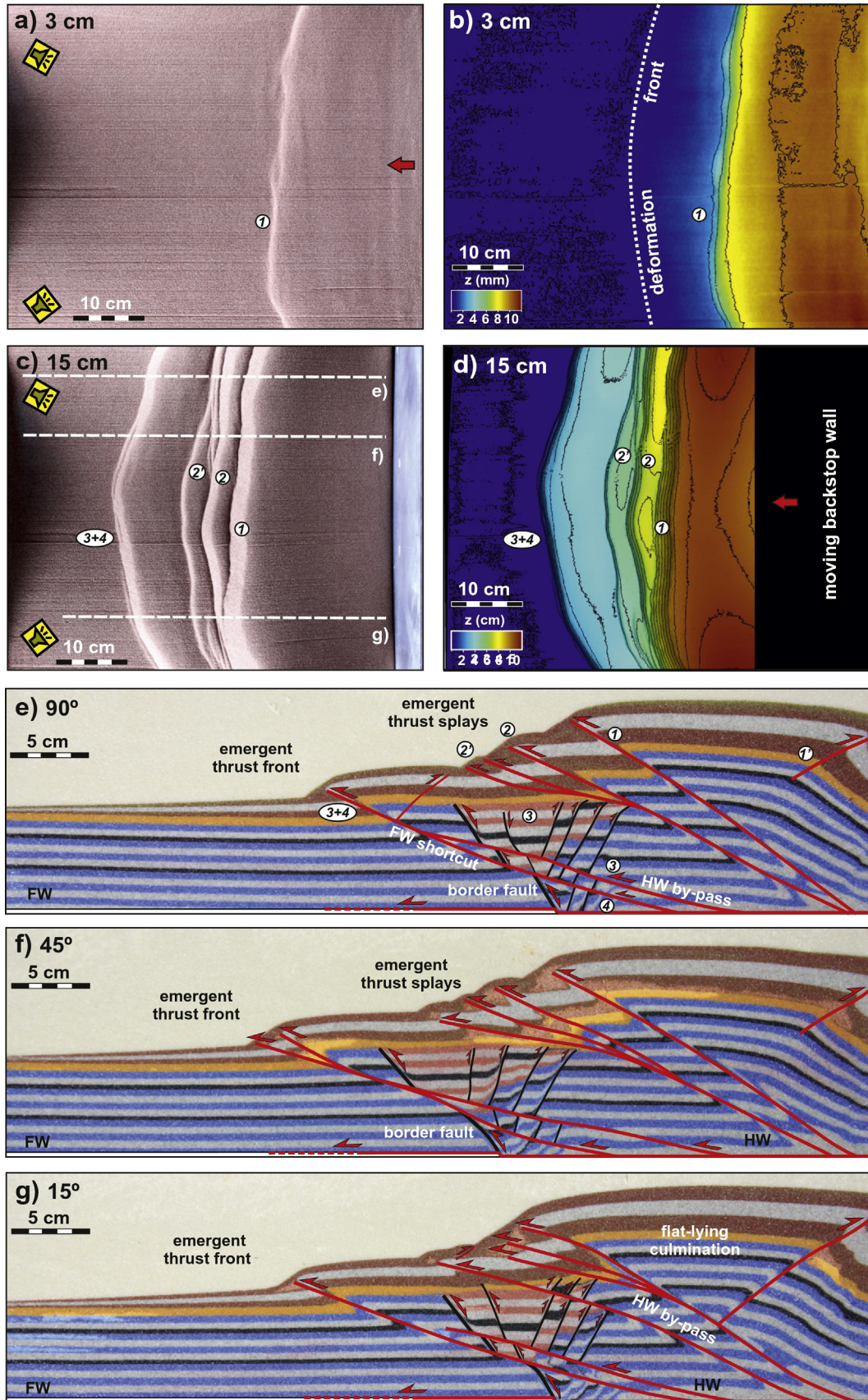
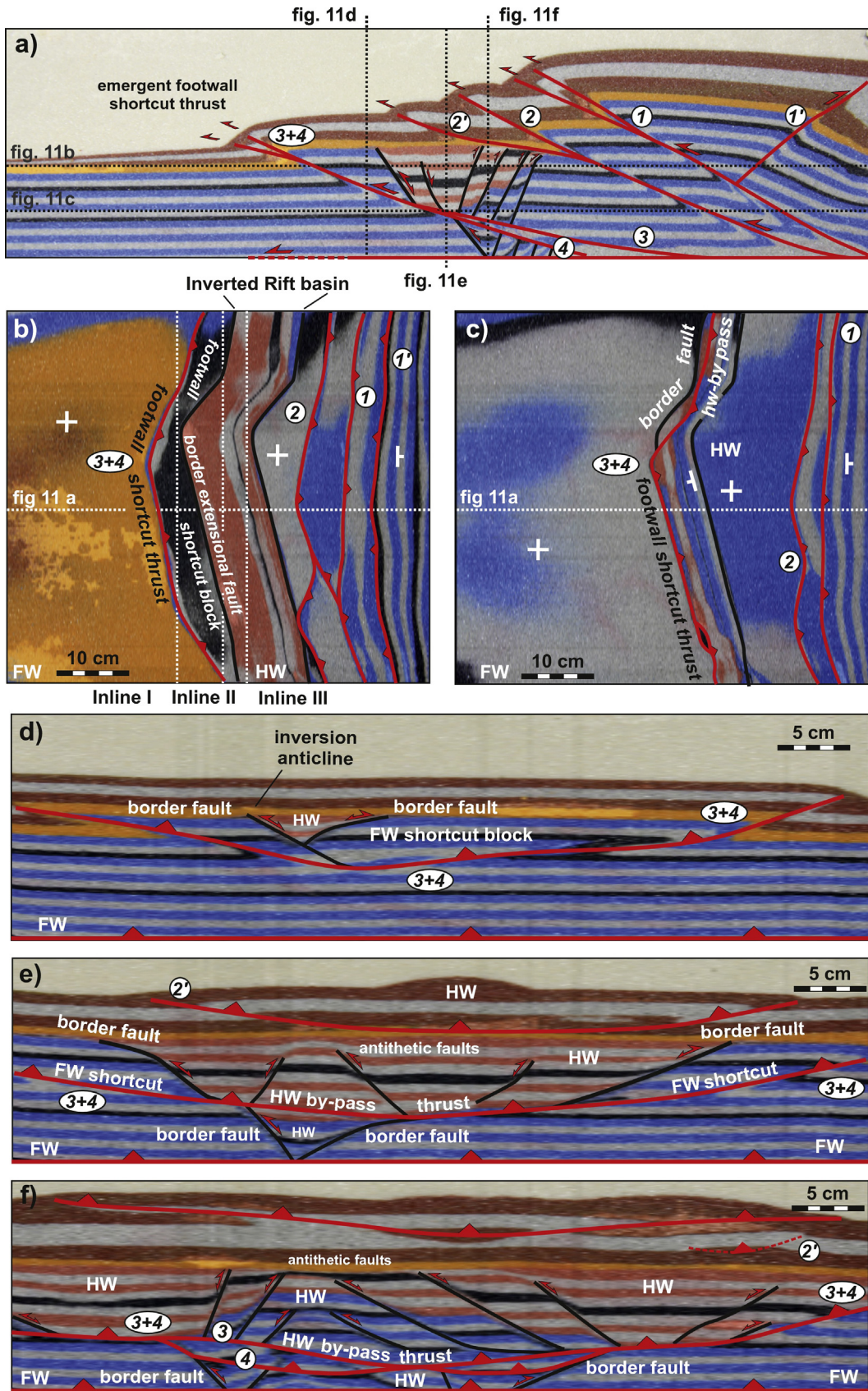
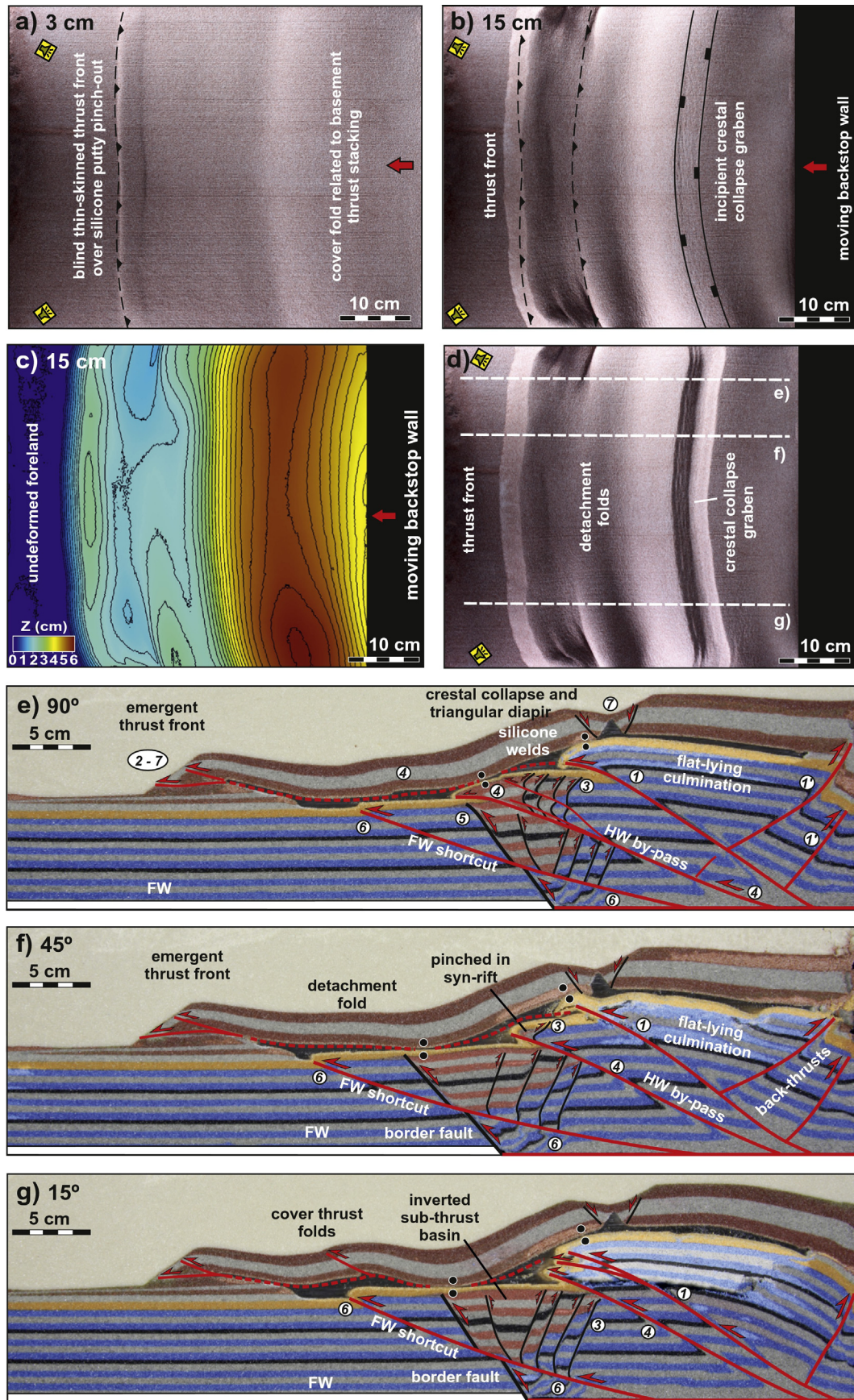


Fig. 11. Summary of results for Model 5. Illumination is from the left. a) Top view after 3 cm of shortening. b) Topography scan after 3 cm. c) Top view at the end of the experiment after 15 cm. d) Topography scan at the end of deformation. e) Cross-section by the 90° segment of the rigid basal plate. f) Cross-section passing by the 45° segment. g) Cross-section by the 15° segment. Numbers indicate relative timing of fault activity. FW: Footwall. HW: Hanging-wall.



**Fig. 12.** Virtual sections extracted from the 3D voxel of Model 5. a) Cross-section for reference. b) Depth-slice using the undeformed post-rift unit (i.e., orange layer) as reference. c) Depth-slice taking the middle of the pre-rift sandpack showing the frontal thrust splitting the half-graben basin in two at the 45° and 90° segments. d) Inline-section showing the footwall shortcut block beneath the imbricated half-graben basin. e) Inline-section showing the imbricated half-graben basin over the hanging-wall by-pass thrust f) Inline-section showing the imbricated half-graben basin in a sub-thrust position. Numbers indicate relative timing of fault activity. FW: Footwall. HW: Hanging-wall.



**Fig. 13.** Summary of results for Model 6. Illumination is from the left. a) Top view after 3 cm of shortening. b) Top view after 15 cm of shortening and c) its topography scan. d) Top view of the model after cessation of shortening. e) Cross-section by the 90° segment of the rigid basal plate. f) Cross-section by the 45° segment. g) Cross-section by the 15° segment. The numbers indicate the relative timing of fault activity. FW: Footwall. HW: Hanging-wall.

#### 4.2.4. Shortening Model 5

This model consisted on the deformation of the segmented half-graben basin along a hinterland dipping basal detachment ( $\beta = 3^\circ$ ) with a sand wedge covering the full stretch of model. The wedge was built with no surface slope (i.e.,  $\alpha = 0^\circ$ ). The pre-shortening configuration of the model is summarised in Fig. 5e. After 15 cm of shortening, time-lapse photography (see online Supplementary material), topography scans and serial cross sections (Fig. 11) showed that the sandbox model was deformed by a dominantly breaking-forwards sequence of thrusting. Time-lapse photography highlighted a significant amount of sand compaction by slip along the hinterland-dipping basal detachment prior to the nucleation of thrusts. Displacement along these thrusts formed several surface-breaching thrust faults and related splays. The compaction of sand by slip along the basal detachment formed a compaction front that advanced ahead of the location of the first emergent thrust front (i.e., thrusts #1 and #2 - #2'). This first sand compaction affected only those layers on the hanging-wall of the extensional basin. Further slip along the basal detachment generated additional compaction of sand ahead of the former compaction front, and in a similar fashion, before the nucleation of additional thrusts (i.e., thrusts #3 and #4). The first and second thrusts to form (i.e., thrusts #1 and #2 - #2') are responsible for the main uplift of the wedge, whereas the last thrust system to develop (i.e., thrusts #3 and #4) imbricated the segmented half-graben basin, and widened the tectonic wedge (Fig. 11). Serial cross sections (Fig. 11e–g) showed that the first three thrust faults developed closely space apart, whereas the last thrust emerged further outboard.

Post-deformation vertical sectioning revealed the subtle reactivation of the extensional faults (i.e., the synthetic and antithetic faults; Fig. 11e–g) and back-thrusting affecting thrust sheet #1. The last thrust faults to form (i.e., thrusts #3 and #4) nucleated also from the rear of the sandpack but propagated through the half-graben basin hanging-wall and footwall. The extensional basin was split by these late thrusts into several segments and was imbricated along with a footwall shortcut block (Fig. 11e–g). In the light of the cross-sections and the lateral time-lapse photography, the sand compaction in between the development of thrusts #1-2-2' and #3-4 seems to be the responsible for the mild inversion of the extensional fault system.

Virtual depth-slices were generated using the undeformed 'foreland' post-rift and pre-rift sand layers as a regional reference of elevation (Fig. 12a–c). The first depth-slice revealed the shape of uplifted half-graben basin, the plan view geometry of the frontal thrusts #3 and #4 and their imbricated footwall fault block. In a similar fashion to the 3D voxel of the baseline extensional model (Fig. 7), the imbricated half-graben basin displays its characteristic shape arranged in the three  $90^\circ$ ,  $45^\circ$  and  $15^\circ$  segments. The footwall shortcut thrust displays kinked plan view geometry, with one larger linear segment parallel to the  $15^\circ$  segment of the border extensional fault, and a shorter sinuous segment striking oblique to the  $45^\circ$  and  $90^\circ$  segments. A deeper depth-slice using the undeformed pre-rift layers as an elevation datum (Fig. 12c) showed a thin slice of the lowermost part of the half-graben basin and its border extensional fault in a sub-thrust footwall position. The geometry of the footwall shortcut thrust is parallel to the trace of the segmented border fault. Virtual inlines generated from the 3D voxel were selected from the foreland towards the hinterland (Fig. 12d–f, respectively). These inlines show the geometry of the footwall shortcut block, along with a fragment of the former segmented half-graben. Gentle anticlines on the hanging-wall of the border fault are indicative for the mild inversion of the segmented extensional fault system. A thin sliver of syn-rift sediments in a footwall position is also revealed by these virtual inlines (Fig. 12e). Thrusts can be correlated along strike

of the sandbox model and display a characteristic concave-upwards geometry.

#### 4.2.5. Shortening Model 6

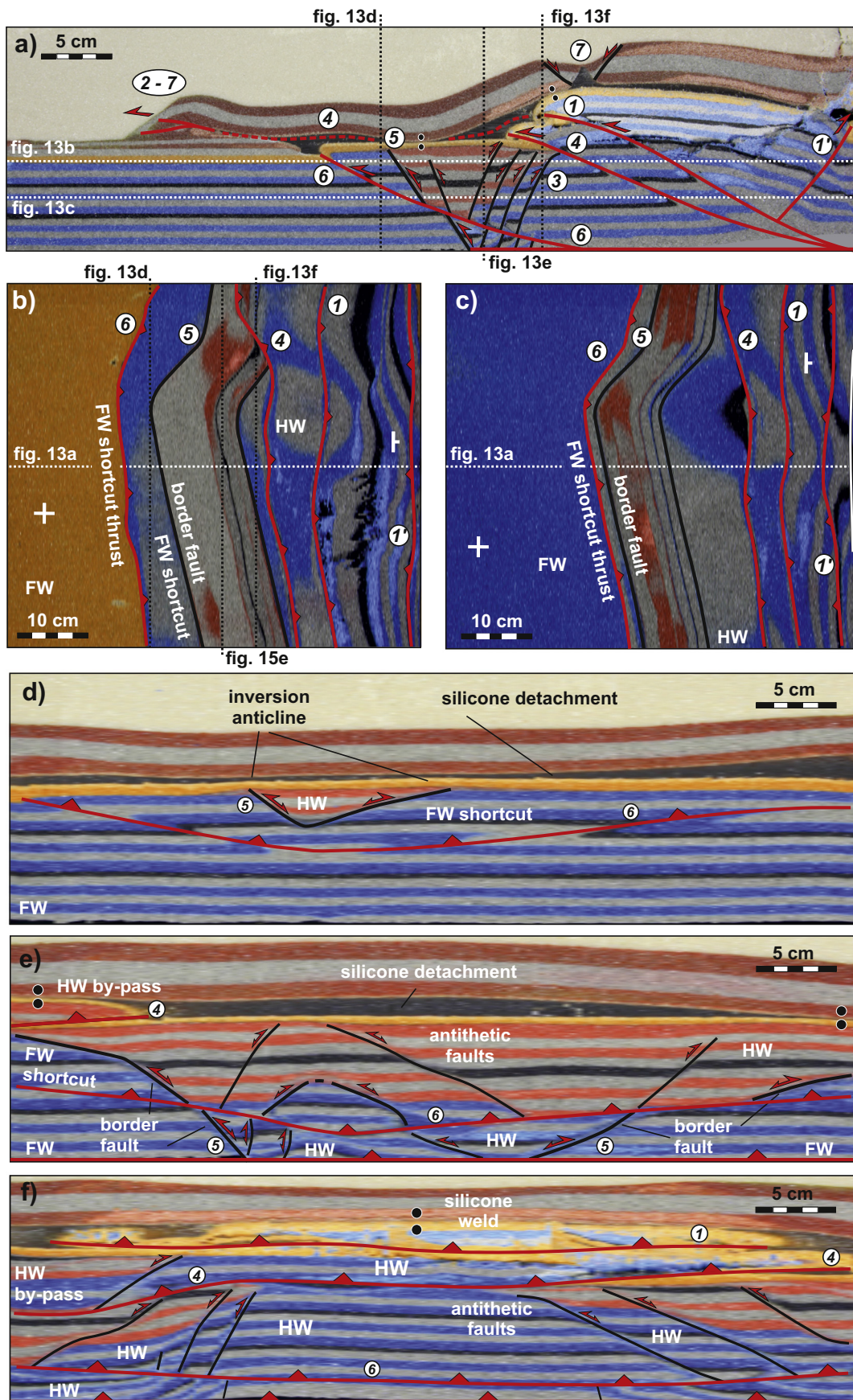
This model also consisted on the deformation of the segmented half-graben basin using the same wedge geometry as that of Model 5 (i.e.,  $\beta = 3^\circ$  and  $\alpha = 0^\circ$ ), but included a 0.4 cm thick layer of viscous polymer. The polymer was laid pinching out in the foreland on a post-rift equivalent stratigraphic position (Fig. 5f). Total shortening was also 15 cm. As shortening started, a first thrust nucleated at the rear of the wedge (i.e., thrust #1) and transferred displacement forwards and upwards along a ramp-flat transition into the viscous polymer layer (i.e., thrust #2). In the early stages of shortening a broad cover anticline was developed above the rearmost thrust, whereas displacement along the viscous detachment formed an emergent thrust front at the polymer's pinch out (Fig. 13a). Further shortening was accommodated by a breaking-forward system of thrusts that affected the sub-polymer layers (i.e., thrusts #4 and #6). Conversely, deformation in the cover was represented by long-lasting deformation at the front, followed by out-of-sequence thrusting and related folding (Fig. 13b).

Contrary to the other shortening models, time-lapse photography has shown that no significant compaction of the sand wedge took place during the early deformation stages (see online Supplementary material). In addition, no evidences of fault reactivation and basin inversion were observed on the top view time-lapse photography during this early deformation. Gentle compaction of the sub-polymer layers took place only after a significant amount of shortening was accommodated by thrusting at the rear and shortening of the overburden along the viscous detachment. Topography scans have also revealed that uplift was mostly concentrated at the rear by the stacking of sub-polymer internal thrust sheets (Fig. 13c). This uplift was responsible for the development of an incipient crestal collapse graben above the frontal culmination of the thrust stack (Fig. 13d). On the other hand, shortening accommodated by the shallow detachment widened the tectonic wedge without generating significant uplift. After cessation of shortening, the uplifted hinterland underwent foreland-ward collapse of the cover units above the polymer layer (Fig. 13d). In this process, the overburden was not fully pierced by the flowing polymer as several welds were developed. These welds are located on top of the half-graben basin and on the frontal culmination of the hinterland thrust stack as shown by the cross-sections (Fig. 13e–g). Extension in the hinterland summit was accommodated by additional down-slope shortening and the associated reactivation of the cover thrust system.

Serial cross-sections have shown that mild inversion of the extensional fault system took place (Fig. 13e–g). Although fault reactivation was preferentially focused on the antithetic faults, the border and synthetic extensional faults were mildly reactivated as well. The observed cross-cutting relationships indicate that reactivation of the extensional faults took place before the imbrication of the segmented half-graben by the sub-polymer thrusts #4 and #6. At the light of the observations made, mild inversion of the extensional faults should have taken place by slip along the basal detachment prior to the break-forward propagation of thrusts #4 and #6. Thrust #4 propagated as a hanging-wall bypass thrust, whereas thrust #6 propagated as a footwall shortcut thrust.

Virtual depth-slices and inline-sections were generated from the 3D voxel (Fig. 14). These sections illustrate further the geometry of the sub-polymer thrust system and the inversion-related structures. The most important observations derived from the voxel data are: in the upper parts of the model (Fig. 14b), the hanging-wall by-pass thrust

**Fig. 14.** Virtual sections extracted from the 3D voxel of Model 6. a) Cross-section for reference. b) Depth-slice taking the undeformed post-rift unit (i.e., orange layer) as reference. c) Depth-slice using the middle of the pre-rift sandpack as reference. d) Inline-section showing the inverted half-graben basin and the footwall shortcut block beneath the polymer detachment. e) Inline-section showing the imbricated sub-thrust basin. f) Inline-section showing thrust-stacking relationships and a large polymer weld. Numbers indicate the timing of thrust movement and basin inversion. FW: Footwall. HW: Hanging-wall.



(i.e., thrust #4) was only developed at the 90° segment. On the other hand, this thrust runs parallel to the 15° segment of the half-graben, and is oblique to the strike of the 45° segment. In the deeper sections (Fig. 14c), thrust #4 displays a rather linear strike. Thrust #6 developed as a footwall shortcut thrust parallel to the border extensional fault, particularly at the lower parts of the model (Fig. 14c). Inline sections have shown the concave-upwards geometry of the shortcut thrust block with a slice of the imbricated basin (Fig. 14d). Gentle hanging-wall anticlines above the reactivated border extensional fault can also be appreciated. A syn-rift repetition is observed associated with the hanging-wall by-pass thrust (i.e., thrust #4), being also located below the polymer detachment (Fig. 14e). The last inline also shows the stacking of thrust #1, #4 and #6 displaying repetitions of pre-rift on top of pre-rift and pre-rift on top of syn-rift. These sections also show the lateral terminations of thrust sheets and related hanging-wall anticlines (Fig. 14f). Polymer welds have also been revealed above the half-graben basin (Fig. 14a, d), on top of the anticline associated with the hanging-wall by-pass thrust (Figs. 13e and 14e), and at the frontal culmination of the hinterland thrust stack (Figs. 13e and 14f).

**5. Discussions**

*5.1. Extension on segmented half-graben basins*

Extension above a segmented velocity discontinuity developed a through-going, segmented border fault along the whole width of the models. On the onset of extension, a fault scarp was formed above the 15° and 90° fault segments to the extension direction; conversely, a

monocline was formed in between, over the fault segment striking at 45° to the extension direction. The initial development of secondary antithetic and synthetic extensional faults consisted on short and isolated arrays. As extension continued, antithetic faults lengthened by tip-propagation, forming relay ramps that were eventually breached and linked to form longer strike, through-going faults. Cross sections have shown different spacing and number of antithetic faults (i.e., fault densities) in the hanging-wall layers of the segmented half-graben (Figs. 6 and 7). A larger number of narrowly-spaced antithetic faults were developed at the 90° and 15° segments to the extension direction, whereas a lower number of steeper and widely-spaced faults developed at the central 45° segment. As shown by time-lapse photography, the extensional displacement along the border faults was continuously concentrated within dilatant but discrete deformation zones. Within these zones, sand grains underwent reorganisation and disaggregation, through rolling and translation by sliding along their contacts. This deformation mechanism is comparable to a particulate or granular flow (e.g., Fossen, 2010) and may have accounted for localised strain-softening. A similar deformation mechanism should be expected for the second order antithetic and synthetic faults.

*5.2. Reactivation and inversion of segmented sub-thrust basins*

The experimental set up provided a good comparison with natural collisional foredeep settings as it effectively simulated the steepening of fault systems in foreland plates as fold-and-thrust belts propagate. According to theoretical and field studies, the steepening of these faults should significantly impact their easiness for frictional reactivation,

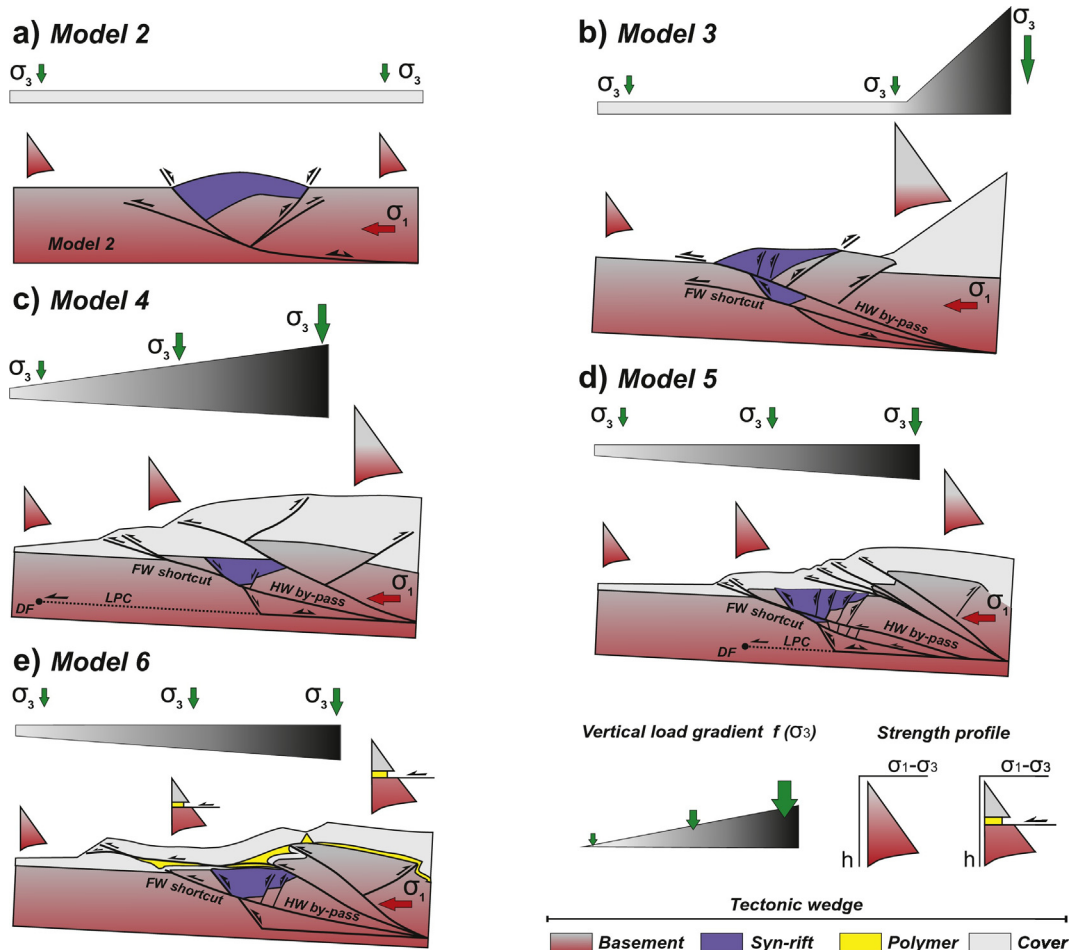


**Fig. 15.** Conceptual summary of the modelling results expressed as a function of the vertical load gradient of the wedge's minimum vertical compressive stress ( $\sigma_3$ ) and the integrated strength profile. DF: deformation front. LPC: layer-parallel compaction.  $\sigma_1$ - $\sigma_3$  = differential stress. h: wedge's thickness. FW: Footwall. HW: Hanging-wall.

particularly in a dip slip reactivation mode (e.g., Jaeger and Cook, 1979; Etheridge, 1986; Gillcrist et al., 1987). In this study, time-lapse photography has shown that, with the exception of Model 4, reactivation of the extensional fault system was mild but affected all models equally along strike, independently of their steep dips. In fact, no substantial differences on the easiness of reactivation regarding of the obliquity between the pre-existing faults (i.e., the 15°, 45° and 90° segments) and the direction of shortening have been found. The obtained modelling results are in disagreement with those reported by Brun and Nalpas (1996) stating the fundamental role of obliquity in the easiness for reactivation.

In all the shortening models, slip along the basal detachment produced different degrees of sand compaction before the onset of thrusting and in between pulses of thrust propagation. For granular analogue materials, Koyi et al. (2004) referred to layer-parallel compaction as the main modality of layer-parallel shortening. The shortening models carried out for this study have shown that the reactivation of the extensional fault system was associated with such layer-parallel compaction, also taking place before the onset of thrusting and in between thrust propagation pulses. The reactivation of the segmented extensional fault system may have been favoured by the dilatant nature of the inherited, strain-softened extensional fault zones. In this sense, Eisenstadt and Sims (2005) reported mild reactivation of a half-graben border fault in relation with the preservation of fault zone dilatancy. A localised loss in the frictional strength (i.e., strain-softening) associated with these discrete fault zones is the most reasonable way to explain how these were reactivated independently of their steep dips and their obliquity with the direction of shortening. In the models carried out, the footwall shortcut thrusts developed broadly parallel to the master border fault (see depth-slices in Figs. 12 and 14), and thus indicate a certain degree of control in the development of thrust systems imposed by the inherited fault zones.

Upon shortening, the models underwent different amounts of layer-parallel compaction, fault-reactivation, thrust propagation and thrust-related folding strictly as a function of the pre-shortening configuration of the tectonic wedge (Fig. 5). The distinctly tapered wedges (i.e.,  $\alpha$  and  $\beta$  angles) affected the reactivation and the incorporation of the sub-thrust basin by imposing a vertical-load gradient on the buried half-graben basins and by their integrated strength profile, which included the strain-softened extensional fault zones and the presence or absence of a shallow viscous detachment. More specifically, the post-rift equivalent 'stratigraphic' position of the viscous layer allowed for the decoupling of deformation between the segmented half-graben and its cover. When the half-graben basin was close to the surface (i.e., Models 2 and 3), inversion of the extensional fault system took place early in the deformation sequence (Figs. 8 and 9). In these two models, the absence of any substantial vertical load (Model 2) or a large vertical load gradient (Model 3) under a dominantly compressional stress field, favoured the reactivation of the extensional fault system during layer-parallel compaction and the earliest onset of thrust propagation, respectively (Fig. 15a, b). When the half-graben basin was covered by a thick wedge (i.e., Model 4, Fig. 10), only the border antithetic fault underwent very limited reactivation by back-thrusting (Fig. 15c). Although the layer-parallel shortening propagated ahead of the half-graben basin, it seems that the large vertical load imposed by the thick wedge hampered or avoided the reactivation of the extensional fault array. On the other hand, when the half-graben basin was covered by a thin wedge (i.e., Model 5; Fig. 11), reactivation of the extensional faults took place late in the deformation sequence, following the breaking-forward propagation of thrusting (Fig. 15d). When the half-graben basin was covered by a thin wedge involving a viscous detachment (i.e., Model 6; Fig. 13), the propagation of thrusting was quickly transferred along a thrust flat towards the foreland overriding the half-graben basin (Fig. 15e). In Model 6, fault reactivation and basin inversion only took place after the

propagation of deformation along the viscous polymer, and hence, later than in the other models.

### 5.3. Comparison to the Höflein high

A comparison between Model 6 and the Höflein high from the sub-thrust of the Alpine-Carpathian fold-and-belt (Fig. 16) has been carried out. Basin inversion in the Alpine-Carpathian fold-and-thrust belt took place in the latest stages of shortening, following the emplacement of a cover thin-skinned thrust system. In Austria, the shallow units of the strongly imbricated Rhenodanubian Flysch are folded into a broad open syncline whereas the Alpine Basal Thrust is folded into an open anticline over the Höflein high (Fig. 16a). These features indicate that the compressional reactivation of the faults in the crystalline basement took place after the emplacement of the shallow, thin-skinned thrust system. Model 6 showed a similar evolution as shown by a fast propagation of slip in the cover that overrode the half-graben along the viscous detachment. This was followed by basin inversion and thrust propagation in the layers beneath the viscous detachment, folding the cover thrust-related folds. In this model, the sequence of basement-involved deformation started with the mild inversion of the extensional fault system in relation with slip along the frictional basal detachment and the associated layer-parallel compaction. In a similar fashion to the natural prototype, reactivation of the inherited extensional fault system was mild, and much of the shortening was accomplished afterwards by the formation and propagation of a new thrust system in the form of foot-wall shortcut thrusts.

### 5.4. Inheritance in natural systems

The reactivation of inherited fault systems is inherent to the concept of basin inversion. In natural systems though, a series of competing geological processes may impact positively or negatively (i.e., enhance or decrease) the role of inheritance. In shallow crustal levels, reactivation is controlled by frictional processes which depend upon the cohesion,

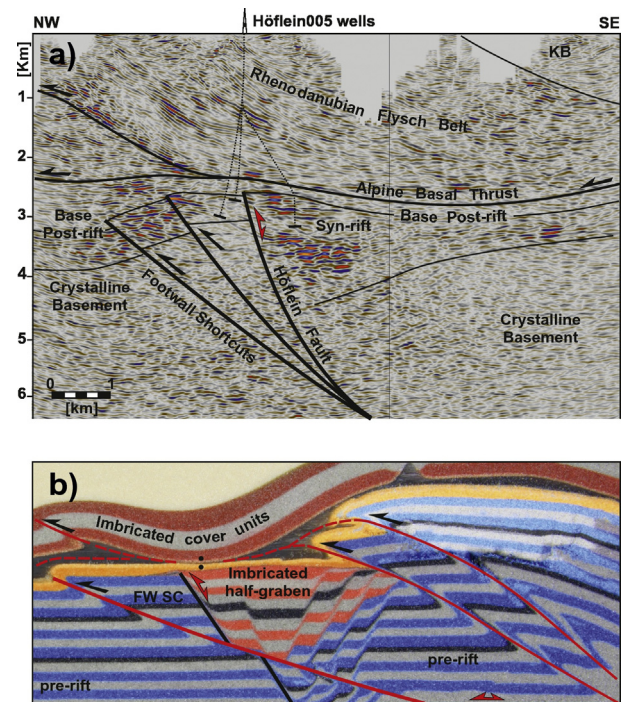


**Fig. 16.** Comparison between the Höflein high and results from Model 6. a) NW-SE striking seismic profile (i.e., approximately parallel to the direction of early Miocene shortening and perpendicular to the basement fault trend). See Fig. 3a for location of the profile. Wells are projected. KB: Korneuburg Basin. b) Cross-section along Model 6. FW SC: Footwall shortcut.

the coefficient of friction, fault orientation (i.e., amount of dip and direction of dip), as well as the pore-fluid pressure (Jaeger and Cook, 1979). Fault-weakening process involving chemical reactions between circulating fluids and the host fault-rocks can induce the formation of low-friction phyllosilicate-rich mineral assemblages (e.g., Gueydan et al., 2003). Therefore, fault-weakening may allow faults to sustain significant slip under theoretically anomalous orientations in respect to the active stress field (e.g., Colletini et al., 2009). These processes may seal faults but otherwise reinforce the role of inheritance, favouring their frictional reactivation. Alternatively, precipitation of hydrothermal fluids, quenching of melts, or widespread brecciation and fracturing within fault zones may favour their frictional lock-up by increasing the coefficient of friction and cohesion (e.g., Etheridge, 1986; Cox et al., 2001). These strain-hardening mechanisms may delocalise deformation and therefore reduce the role of inheritance in natural systems.

## 6. Conclusions

The experimental results indicate that the key parameters controlling the inversion of sub-thrust extensional basins are the wedges' vertical load and its pre-shortening integrated strength profile (Fig. 15). Large vertical loads hamper the inversion of deeply buried basins, whereas lower vertical loads or high vertical load gradients may favour the inversion of sub-thrust basins by fault reactivation and thrust propagation. Integrated strength profiles included the presence of discrete, strain-softened fault zones inherited from the extensional phases, as well as the presence/absence of viscous layers. The obliquity between the shortening direction and the orientation of pre-existing faults seemed less important than the vertical load distribution and the fault zone strength for the inversion of sub-thrust basins. Natural processes that modify the regional slope of tectonic wedges (i.e., such as erosion and sedimentation) should therefore have strong impacts on the likelihood and timing of sub-thrust basin inversion.

Fault reactivation occurred during layer-parallel compaction before and in between thrust propagation pulses associated with slip along the basal detachment of the system. Widespread, laterally extensive (i.e., post-rift) viscous layers may favour an early decoupling between cover and basement during shortening, with basin inversion taking place after the imbrication of cover units. A certain control imposed by the inherited extensional architecture in the formation of shortcut thrusts is also suggested by the results. Sandbox analogue modelling coupled with time-lapse photography, white-light topography scans, and serial sections from imaged-based 3D voxels have revealed as great tools for the better understanding of basin inversion in tectonic wedges.

## Acknowledgements

This is a contribution of the Institut de Recerca Geomodels and the Geodinàmica i Anàlisi de Conques research group (2014SGR467SGR) from the Agència de Gestió d'Ajuts Universitaris i de Recerca (AGAUR) and the Secretaria d'Universitats i Recerca del Departament d'Economia i Coneixement de la Generalitat de Catalunya. The Geomodels Analog Modelling Laboratory was supported by a Scientific Infrastructure (UNBA08-4E-006) co-funded by the European Regional Development Fund of the *Ministerio de Ciencia e Innovación* of the Spanish Government and Statoil. PG acknowledges financial support, data supply and permission to publish from OMV Exploration and Production GmbH (Project FBG307451). Financial support from SALTECRES (CGL2014-54118-C2-1-R) project is also acknowledged. The final version of this manuscript benefited from the constructive reviews of Dr. João C. Duarte (Univ. of Lisbon), Dr. Stephane Dominguez (Univ. of Montpellier) as well as the Editor-in-Chief Dr. Philippe Agard (Univ. Université Pierre et Marie Curie, Sorbonne Universités, Paris). Modelling software Petrel by Schlumberger and Skua by Paradigm were used for seismic interpretation, 3D model building and analysis of laser-scanner data. Move

restoration software by Midland Valley was used for cross-section construction.

## Appendix A. Supplementary data

Supplementary data to this article can be found online at <http://dx.doi.org/10.1016/j.tecto.2017.02.022>.

## References

- Adam, J., Urai, J., Wieneke, B., Oncken, O., Pfeiffer, K., Kukowski, N., Lohrmann, J., Hoth, S., van der Zee, W., Schmatz, J., 2005. Shear localisation and strain distribution during tectonic faulting - new insights from granular flow experiments and high-resolution optical image correlation techniques. *J. Struct. Geol.* 27, 283–301.
- Bartholomew, I.D., Peters, J.M., Powell, C.M., 1993. Regional structural evolution of the North Sea: oblique slip and the reactivation of basement lineaments. *Petroleum Geology Conference series 4*. Geological Society of London: pp. 1109–1112. <http://dx.doi.org/10.1144/0041109>.
- Beidinger, A., Decker, K., 2014. Quantifying Early Miocene in-sequence and out-of-sequence thrusting at the Alpine-Carpathian junction. *Tectonics* 33, 222–252.
- Bonini, M., 2007. Deformation patterns and structural vergence in brittle-ductile thrust wedges: an additional analogue modelling perspective. *J. Struct. Geol.* 29, 141–158.
- Bonini, M., Sani, F., Antonielli, B., 2012. Basin inversion and contractional reactivation of inherited normal faults: a review based on previous and new experimental models. *Tectonophysics* 522–523, 55–88.
- Bonnet, C., Malavieille, J., Mosar, J., 2007. Interactions between tectonics, erosion, and sedimentation during the recent evolution of the Alpine orogen: analogue modelling insights. *Tectonics* 26. <http://dx.doi.org/10.1029/2006TC002048>.
- Brun, J.P., Nalpas, T., 1996. Graben inversion in nature and experiments. *Tectonics* 15, 677–687.
- Buchanan, P.G., McClay, K.R., 1991. Sandbox experiments of inverted listric and planar fault systems. In: Cobbold, P.R. (Ed.), *Experimental and Numerical Modelling of Continental Deformation: Tectonophysics*. 188, pp. 97–115.
- Buchanan, P.G., McClay, K.R., 1992. Experiments on basin inversion above reactivated domino faults. *Mar. Pet. Geol.* 9, 486–500.
- Buiter, S., Pfiffner, O.A., Beaumont, C., 2009. Inversion of extensional sedimentary basins: a numerical evaluation of the localization of shortening. *Earth Planet. Sci. Lett.* 288, 492–504.
- Carrera, N., Muñoz, J.A., 2013. Thick-skinned tectonic style resulting from the inversion of previous structures in the southern Cordillera Oriental (NW Argentine Andes). In: Nemčok, M., Mora, A., Cosgrove, J.W. (Eds.), *Thick-skinned Dominated Orogens: From Initial Inversion to Full Accretion*. 377. Geological Society of London, pp. 119–140 (Special Publication).
- Chapple, W.M., 1978. Mechanics of Thin-Skinned Fold-and-Thrust Belts. *Geol. Soc. Am. Bull.* 89, 1189–1198.
- Colletini, C., Niemeijer, A., Viti, C., Marone, C., 2009. Fault zone fabric and fault weakness. *Nature* 462:907–910. <http://dx.doi.org/10.1038/nature08585>.
- Couzens-Schultz, B.A., Vendeville, B.C., Wiltschko, D.V., 2003. Duplex style and triangle zone formation: insights from sandbox analogue physical modelling. *J. Struct. Geol.* 25, 1623–1644.
- Cox, S.F., Knacksedt, M.A., Braun, J., 2001. Principles of structural control on permeability and fluid flow in hydrothermal systems. In: Richards, J.P., Tosdal, R.M. (Eds.), *Structural Controls on Ore Genesis. Reviews in Economic Geology, Reviews 14*. Society of Economic Geologists Inc., Littleton, USA, pp. 1–22.
- D'Adda, P., Longoni, R., Magistroni, C., Meda, M., Righetti, F., Cavozzi, C., Nestola, Y., Storti, F., 2017. Extensional reactivation of a deep transpressional architecture: insights from sandbox analogue modeling applied to the Val d'Agri basin (Southern Apennines, Italy). *Interpretation* 5 (1):SD55–SD66. <http://dx.doi.org/10.1190/INT-2016-0078.1>.
- Davy, P., Cobbold, P.R., 1991. Experiments of shortening of a 4-layer model of the continental lithosphere. *Tectonophysics* 188, 1–25.
- Decker, K., Peresson, H., 1996. Tertiary kinematics in the Alpine-Carpathian-Pannonian system: links between thrusting, transform faulting and crustal extension. In: Wessely, G., Liebl, W. (Eds.), *Oil and Gas in Alpidic Thrustbelts and Basins of Central and Eastern Europe*. 5. Geological society, London, pp. 69–77 (EAGE Special Publication).
- Del Ventisette, C., Montanari, D., Sani, F., Bonini, M., 2006. Basin inversion and fault reactivation in laboratory experiments. *J. Struct. Geol.* 28, 2067–2083.
- Dell'Ertola, D., Schellart, W.P., 2013. The development of shear folds in viscously stratified materials in simple shear conditions: an analogue approach. *J. Struct. Geol.* 56, 129–141.
- Di Domenica, A., Bonini, L., Calamita, F., Toscani, G., Galuppo, C., Seno, S., 2014. Analogue modeling of positive inversion tectonics along differently oriented pre-thrusting normal faults: an application to the Central-Northern Apennines of Italy. *Geol. Soc. Am. Bull.* <http://dx.doi.org/10.1130/B31001.1>.
- Dooley, T.P., Jackson, M.P.A., Hudec, M.R., 2009. Inflation and deflation of deeply buried salt stocks during lateral shortening. *J. Struct. Geol.* 31, 582–600.
- Dubois, A., Odonne, F., Massonnat, G., Lebourg, T., Fabre, R., 2002. Analogue modelling of fault reactivation: tectonic inversion and oblique remobilization of grabens. *J. Struct. Geol.* 24, 1741–1752.
- Eisenstadt, G., Sims, D., 2005. Evaluating sand and clay models: do rheological differences matter? *J. Struct. Geol.* 27, 1399–1412.
- Eisenstadt, G., Withjack, M.O., 1995. Estimating inversion: results from clay models. In: Buchanan, J.G., Buchanan, P.G. (Eds.), *Basin Inversion*. Geological Society of London Special Publication 88, pp. 119–136.

- El Harfi, A., Guiraud, M., Lang, J., 2006. Deep-rooted “thick skinned” model for the High Atlas Mountains (Morocco). Implications for the structural inheritance of the southern Tethys passive margin. *J. Struct. Geol.* 28, 1958–1976.
- Erdős, Z., Huismans, R.S., van der Beek, P., Thieulot, C., 2014. Extensional inheritance and surface processes as controlling factors of mountain belt structure. *J. Geophys. Res. Solid Earth* 119:9042–9061. <http://dx.doi.org/10.1002/2014JB011408>.
- Etheridge, M.A., 1986. On the reactivation of extensional fault systems. *Philos. Trans. R. Soc. A Math. Phys. Eng. Sci.* 317:179–194. <http://dx.doi.org/10.1098/rsta.1986.0031>.
- Faulds, J.E., Varga, R.J., 1998. The role of accommodation zones and transfer zones in the regional segmentation of extended terranes. In: Faulds, J.E., Stewart, J.H. (Eds.), *Accommodation Zones and Transfer Zones: The Regional Segmentation of the Basin and Range Province*. 323. Geological Society of America, Boulder, pp. 1–46 (Special Paper).
- Fodor, L., 1995. From transpression to transtension: Oligocene-Miocene structural evolution of the Vienna Basin and the East-Alpine-Western Carpathian junction. *Tectonophysics* 242, 151–182.
- Fossen, H., 2010. Deformation bands formed during soft-sediment deformation: observations from SE Utah. *Mar. Pet. Geol.* 27, 215–222.
- Fossen, H., Fazli Khani, H., Faleide, J.J., Ksienzyk, A.K., Dunlap, W.J., 2016. Post-Caledonian extension in the West Norway–northern North Sea region: the role of structural inheritance. In: Childs, C., Holdsworth, R.E., Jackson, C.A.-L., Manzocchi, T., Walsh, J.J., Yielding, G. (Eds.), *The Geometry and Growth of Normal Faults*. 439. Geological Society, London. <http://dx.doi.org/10.1144/SP439.6> (Special Publications).
- Gawthorpe, R.L., Hurst, J.M., 1993. Transfer zones in extensional basins: their structural style and influence on drainage development and stratigraphy. *J. Geol. Soc.* 150 (6), 1137–1152.
- Gibbs, A.D., 1984. Structural evolution of extensional basin margins. *J. Geol. Soc. Lond.* 141, 609–620.
- Gillcrist, R., Coward, M.P.A., Mugnier, J.L., 1987. Structural inversion and its controls: examples from the Alpine foreland and the French Alps. *Geodin. Acta* 1, 5–34.
- Granado, P., Thöny, W., Carrera, N., Gratzler, O., Strauss, P., Muñoz, J.A., 2016. Basement-involved reactivation in fold-and-thrust belts: the Alpine-Carpathian Junction (Austria). *Geol. Mag.* 153 (5–6), 1110–1135.
- Graveleau, F., Malavielle, J., Dominguez, S., 2012. Experimental modelling of orogenic wedges: a review. *Tectonophysics* 538–540, 1–66.
- Gueydan, F., Leroy, Y.M., Jolivet, L., Agard, P., 2003. Analysis of continental midcrustal strain localization induced by reaction softening and microfracturing. *J. Geophys. Res.* 108 (B2):2064. <http://dx.doi.org/10.1029/2001JB000611>.
- Holdsworth, R.E., Stewart, M., Imber, J., Strachan, R.A., 2001. The structure and rheological evolution of reactivated continental fault zones: a review and case study. In: Miller, J.A., Holdsworth, R.E., Buick, I.S., Hand, M. (Eds.), *Continental Reactivation and Reworking*. 184. Geological Society of London, pp. 115–137 (Special Publication).
- Hölzel, M., Decker, K., Zámolyi, A., Strauss, P., Wägrich, M., 2010. Lower Miocene structural evolution of the central Vienna Basin (Austria). *Mar. Pet. Geol.* 27, 666–681.
- Horváth, F., Bada, G., Szafián, P., Tari, G., Ádám, A., Cloetingh, S., 2006. Formation and deformation of the Pannonian Basin: constraints from observational data. In: Gee, D.G., Stephenson, R.A. (Eds.), *European Lithosphere Dynamics*. 32. Geological Society, Memoirs, London, pp. 191–206.
- Hubbert, M.K., 1951. Mechanical basis for certain geological structures. *Geol. Soc. Am. Bull.* 62, 355–372.
- Huismans, R.S., Podladchikov, Y.Y., Cloetingh, S., 2001. Dynamic modelling of the transition from passive to active rifting, application to the Pannonian Basin. *Tectonics* 20: 1021–1039. <http://dx.doi.org/10.1029/2001TC900010>.
- Huyghe, P., Mugnier, J.L., 1995. A comparison of inverted basins of the Southern North Sea and inverted structures of the external Alps. In: Buchanan, J.G., Buchanan, P.G. (Eds.), *Basin Inversion*. 88. Geological Society of London, pp. 339–354 (Special Publication).
- Jaeger, G.D., Cook, N.G.W., 1979. *Fundamentals of Rock Mechanics*. Chapman & Hill Ltd, London (515pp).
- Koopman, A., Speksnijder, A., Horsfield, W.T., 1987. Sandbox models of inversion tectonics. *Tectonophysics* 137, 379–388.
- Koyi, H.A., Sans, M., Teixell, A., Cotton, J., Zeyen, H., 2004. The significance of penetrative strain in the restoration of shortened layers—insights from sand models and the Spanish Pyrenees. In: McClay, K.R. (Ed.), *Thrust Tectonics and Hydrocarbon Systems: AAPG Memoir*. 82, pp. 207–222.
- Lohrmann, J., Kukowski, N., Adam, J., Oncken, O., 2003. The impact of analogue material properties on the geometry, kinematics and dynamics of convergent sand wedges. *J. Struct. Geol.* 25, 1691–1711.
- Malavielle, J., 2010. Impact of erosion, sedimentation, and structural heritage on the structure and kinematics of orogenic wedges: analogue models and case studies. *GSA Today* 20, 4–10.
- McClay, K.R., 1989. Analogue models of inversion tectonics. In: Cooper, M.A., Williams, G.D. (Eds.), *Inversion Tectonics*. 44. Geological Society of London, pp. 41–62 (Special Publication).
- McClay, K.R., 1995. The geometries and kinematics of inverted fault systems: a review of analogue model studies. In: Buchanan, J.G., Buchanan, P.G. (Eds.), *Basin Inversion*. 88. Geological Society of London, pp. 97–118 (Special Publication).
- McClay, K.R., 1996. Recent advances in analogue modeling: uses in section interpretation and validation. In: Buchanan, P.G., Nieuwland, D.A. (Eds.), *Modern Developments in Structural Interpretation, Validation and Modelling*. 99. Geological Society of London, pp. 201–225 (Special Publications).
- Mencos, J., Carrera, N., Muñoz, J.A., 2015. Influence of half-graben basin geometry on the subsequent post-rift sedimentation and basin inversion: the Organyà Basin and the Bóixols thrust sheet (south Central Pyrenees). *Tectonics* 34:1452–1474. <http://dx.doi.org/10.1002/2014TC003692>.
- Morley, C.K., 2010. Stress re-orientation along zones of weak fabrics in rifts: an explanation for pure extension in ‘oblique’ rift segments? *Earth Planet. Sci. Lett.* 297: 667–673. <http://dx.doi.org/10.1016/j.epsl.2010.07.022>.
- Morley, C.K., Nelson, R.A., Patton, T.L., Munn, S.G., 1990. Transfer zones in the East African rift system and their relevance to hydrocarbon exploration in rifts (1). *AAPG Bull.* 74 (8), 1234–1253.
- Muñoz, J.A., 2002. Alpine Tectonics I: the alpine system north of the Betic Cordillera tectonic setting; the Pyrenees. In: Gibbons, W., Moreno, T. (Eds.), *The Geology of Spain*. Geological Society, London, pp. 370–385.
- Nilforoushan, F., Pysklywec, R., Cruden, A., Koyi, H., 2013. Thermal-mechanical modelling of salt-based mountain belts with pre-existing basement faults: application to the Zagros fold and thrust belt, southwest Iran. *Tectonics* 32:1212–1226. <http://dx.doi.org/10.1002/tect.20075>.
- Panien, M., Schreus, G., Pfiffner, A.O., 2005. Sandbox experiments on basin inversion: testing the influence of basin orientation and basin fill. *J. Struct. Geol.* 27, 433–445.
- Ratschbacher, L., Frisch, W., Linzer, H.G., Merle, O., 1991. Lateral extrusion in the Eastern Alps, 2. Structural analysis. *Tectonics* 10, 257–271.
- Roure, F., Colletta, B., 1996. Cenozoic inversion structures in the foreland of the Pyrenees and Alps. In: Ziegler, P.A.H., Horvath, F. (Eds.), *Peri-Tethys Memoir 2: Structure and Prospects of the Alpine Basins and Forelands*, 170. Mémoires Muséum National d’Histoire Naturelle, Paris, pp. 173–209.
- Santolaria, P., Vendeville, B.C., Graveleau, F., Soto, R., Casas-Sainz, A., 2015. Double evaporitic décollements: influence on pinch-out overlapping in experimental thrust wedges. *J. Struct. Geol.* 76, 35–51.
- Sassi, W., Colletta, B., Balé, P., Paquereau, T., 1993. Modelling of structural complexity in sedimentary basins: the role of pre-existing faults in thrust tectonics. *Tectonophysics* 226, 97–112.
- Schellart, W.P., 2000. Shear test results for cohesion and friction coefficients for different granular materials: scaling implications for their usage in analogue modelling. *Tectonophysics* 324, 1–16.
- Schellart, W.P., Strak, V., 2016. A review of analogue modelling of geodynamic processes: approaches, scaling, materials and quantification, with an application to subduction experiments. *J. Geodyn.* 100, 7–32.
- Schmid, S.M., Fügenschuh, B., Kissling, E., Schuster, R., 2004. Tectonic map and overall architecture of the Alpine orogen. *Eclogae Geol. Helv.* 97, 93–117.
- Schreurs, G., Buiter, S.J.H., Boutelier, D., Corti, G., Costa, E., Cruden, A.R., Daniel, J.-M., Hoth, S., Koyi, H.A., Kukowski, N., Lohrmann, J., Ravaglia, A., Schlische, R.W., Withjack, M.O., Yamada, Y., Cavozzi, C., Delventisette, C., Elder Brady, J.A., Hoffmann-Rothe, A., Mengus, J.-M., Montanari, D., Nilforoushan, F., 2006. Analogue benchmarks of shortening and extension experiments. In: Buiter, S.J.H., Schreurs, G. (Eds.), *Analogue and Numerical Modelling of Crustal-scale Processes*. 253. Geological Society of London, pp. 1–27 (Special Publication).
- Scisciani, V., 2009. Styles of positive inversion tectonics in the Central Apennines and in the Adriatic foreland: implications for the evolution of the Apennine chain (Italy). *J. Struct. Geol.* 31, 1276–1294.
- Shiner, P., Beccacini, A., Mazzoli, S., 2004. Thin-skinned versus thick-skinned structural models for Apulian carbonate reservoirs: constraints from the Val d’Agri Fields, S. Apennines, Italy. *Mar. Pet. Geol.* 21, 805–827.
- Smit, J.H.W., Brun, J.P., Sokoutis, D., 2003. Deformation of brittle-ductile thrust wedges in experiments and nature. *J. Geophys. Res.* 108. <http://dx.doi.org/10.1029/2002JB002190>.
- Storti, F., McClay, K., 1995. Influence of syntectonic sedimentation on thrust wedges in analogue models. *Geology* 23 (11), 999–1002.
- Strauss, P., Wägrich, M., Decker, K., Sachsenhofer, R.F., 2001. Tectonics and sedimentation in the Fohnsdorf-Seckau basin (Miocene-Austria): from a pull-apart basin to a half-graben. *Int. J. Earth Sci.* 90, 549–559.
- Tomek, Č., Hall, J., 1993. Subducted continental margin imaged in the Carpathians of Czechoslovakia. *Geology* 21, 535–538.
- Vially, R., Letouzey, J., Benard, F., Haddadi, N., Desforges, G., Askri, H., Boudjema, A., 1994. Basin inversion along the North African Margin: the Saharan Atlas (Algeria). In: Roure, F. (Ed.), *Peri-Tethyan Platforms Editions Technip*, Paris, pp. 79–120.
- Wagner, L.R., 1998. Tectono-stratigraphy in the Molasse Foredeep of Salzburg, Upper and Lower Austria. In: Masclé, A., Puigdefàbregas, C., Luterbacher, H.P., Fernández, M. (Eds.), *Cenozoic Foreland Basins of Western Europe*. 134. Geological Society of London, pp. 339–369 (Special Publication).
- Weijermars, R., Jackson, M.P.A., Vendeville, B.C., 1993. Rheological and tectonic modeling of salt provinces. *Tectonophysics* 217, 143–174.
- Weijermars, R., Schmelting, H., 1986. Scaling of Newtonian and non-Newtonian fluid dynamics without inertia for qualitative modelling of rock flow due to gravity. *Phys. Earth Planet. Inter.* 43, 316–330.
- Wernicke, B., Burchfield, B.C., 1982. Models of extensional tectonics. Inaugural meeting of the Canadian Tectonics Group. 4, pp. 105–115.
- Wessely, G., 1987. Mesozoic and Tertiary evolution of the Alpine-Carpathian foreland in eastern Austria. *Tectonophysics* 137, 45–49.
- Williams, G.D., Powell, C.M., Cooper, M.A., 1989. Geometry and kinematics of inversion tectonics. In: Cooper, M.A., Williams, G.D. (Eds.), *Inversion Tectonics*. 44. Geological Society of London, pp. 3–15 (Special Publication).
- Yamada, Y., McClay, K.R., 2004. 3-D analog modelling of inversion thrust structures. In: McClay, K.R. (Ed.), *Thrust Tectonics and Hydrocarbon Systems*. AAPG Memoir 82, pp. 276–301.
- Ziegler, P.A., Cloetingh, S., Guiraud, R., Stampfli, G., 2001. Peri-Tethyan platforms: constraints on dynamics of rifting and basin inversion. In: Ziegler, P.A., Cavazza, W., Robertson, A.H.F., Crasquin-Soleau, S. (Eds.), *Peri-Tethys Memoir 6: Peri-Tethyan Rift/Wrench Basins and Passive Margins*. Mus. Nat. Hist. Nat. 186, pp. 9–49.
- Zimmer, W., Wessely, G., Wessely, G., Liebl, W., 1996. Exploration results in thrust and sub-thrust complexes in the Alps and below the Vienna Basin in Austria. Oil and Gas in Alpidic Thrustbelts and Basins of Central and Eastern Europe. 5. Geological Society, London, pp. 81–107 (EAGE Special Publication).